

A displacement smoothing induced strain gradient stabilization for the meshfree Galerkin nodal integration method

C. T. Wu¹ · M. Koishi² · W. Hu¹

Received: 30 January 2015 / Accepted: 4 April 2015 / Published online: 25 April 2015
© Springer-Verlag Berlin Heidelberg 2015

Abstract In this paper, we present a gradient-type stabilization formulation for the meshfree Galerkin nodal integration method in linear elastic analysis. The stabilization is introduced to the standard variational formulation through an enhanced strain induced by a decomposed smoothed displacement field using the first-order meshfree convex approximations. It leads to a penalization formulation containing a symmetric strain gradient stabilization term for the enhancement of coercivity in the direct nodal integration method. As a result, the stabilization parameter comes naturally from the enhanced strain field and provides the simplest means for effecting stabilization. This strain gradient stabilization formulation is also shown to pass the constant stress patch test if the SCNI scheme is applied to the non-stabilized terms. Several numerical benchmarks are examined to demonstrate the effectiveness and accuracy of the proposed stabilization method in linear elastic analysis.

Keywords Meshfree · Nodal integration · Stabilization

1 Introduction

Meshfree, or particle methods, offer many numerical advantages over conventional finite element and finite difference methods in modeling large deformation, moving discontinuity and immersed problems in solid and structural applications [6,21,22,29,30,40]. Those methods were also found

to be very effective in reducing the volumetric locking and shear locking in solid and structural analyses [10,12,35]. Nevertheless, an application of a direct nodal integration scheme to meshfree or particle methods suffers from the presence of spurious low or zero-energy modes [2] in solid mechanics problems. The presence of spurious energy modes in Galerkin-based meshfree methods mainly emanates from the rank instability caused by the under-integration of weak forms inherent in the central difference formula from the direct nodal integration scheme.

A number of stabilized meshfree Galerkin methods have been developed to suppress the spurious energy modes caused by the direct nodal integration scheme. The Galerkin/least-squares (GLS) stabilization approach [2] presents a reconstructed weak form for the meshfree nodal integration method in which a bilinear term consisting of the residual of equilibrium equation is employed to stabilize the solution. This method enables the solution of partial differential equations only based on a set of nodes without a need of integration cells. Nevertheless, like many finite element stabilization methods, the optimal choice of the stabilization control parameter remains an open question. The so-called physical stabilization technique [25] based on the Taylor-series expansion of displacement gradient matrix for the finite element method is free of stabilization control parameters. This stabilization technique has been applied to several meshfree Galerkin nodal integration methods [8,23]. A common feature of those physical stabilization methods is the usage of higher-order derivatives and integration cells for the meshfree computation. In 2001, Chen et al. [9] developed a stabilized conforming nodal integration (SCNI) method in which the “integration constraint” concept was proposed for the design of an accurate meshfree nodal integration algorithm. Based on the integration constraint, a strain-smoothing scheme was introduced as a stabilization process for nodal

✉ C. T. Wu
ctwu@lstc.com

¹ Livermore Software Technology Corporation, Livermore, CA 94550, USA

² Koishi Laboratory, The Yokohama Rubber Co. Ltd., Tokyo, Japan

integration. This strain-smoothing scheme leads to a consistent formulation that passes the linear exactness in the Galerkin approximation and does not involve the shape function derivatives in computation. The performance of SCNI method was further improved by the introduction of penalty-type of stabilizations [28] to the nonlinear analysis. To enhance the ability of SCNI method in severe deformation analysis, a non-conforming SCNI method [15] was developed. The non-conforming SCNI method combines the semi-Lagrangian reproducing kernels with the mismatching integration cells to allow large strain and failure simulations under the extreme loading conditions. The concept of integration constraint in SCNI method also has been generalized to achieve a quadratic consistent integration scheme [13]. Based on the SCNI technique and the meshfree regularization methodology [7], a two-level Lagrangian nodal gradient smoothing algorithm was recently developed [41] to study the material instability in concrete structures. Most recently, the consistency conditions for arbitrary order exactness in the Galerkin approximation were introduced by Chen et al. [11] to further reduce the solution errors of PDEs from quadrature inaccuracy. Moreover, their method has been shown [18] to remarkably alleviate the unstable deformation mode in the simulation of impact problems.

The robustness and accuracy of meshfree or particle methods in solid and structural analyses are also greatly affected by their numerical treatments of boundary conditions. Since the Kronecker-delta property does not hold in the conventional meshfree approximations such as the moving least-squares (MLS) [3] and reproducing kernel (RK) [26] approximations, special techniques [6, 16, 17, 21, 36] are needed to impose the constraint and essential boundary conditions in meshfree methods. Alternatively, several convex approximations were introduced [1, 31] to simplify the essential boundary condition treatment in meshfree methods. Meshfree convex approximations guarantee the unique solution inside a convex hull with a minimum distributed data set and possesses the Kronecker-delta property at the boundaries to avoid the special numerical treatment on the essential boundaries. Wu et al. [37] have provided a unified approach that can generate specific convex approximations as well as reproduce several existing meshfree approximations. Park et al. [27] embarked on a detailed dispersion analysis and reported that meshfree convex approximation exhibits smaller lagging phase and amplitude errors than meshfree non-convex approximation in full-discretization of the wave equation. Several meshfree Galerkin and meshfree-enriched finite element formulations based on the meshfree convex approximation also have been developed for solid mechanics applications [38, 39].

Despite a lot of research works have been done in stabilizing the meshfree nodal integration method, there is still a need for a robust and accurate stabilization formulation

in solid mechanics applications. In particular, a stabilization formulation that is free of stabilization control parameters and integration cells would minimize the computational complexity and improve the numerical performance in a large extent of meshfree applications. This paper aims to present an alternative stabilized nodal integration method where the direct nodal integration scheme can be used in the computation and the stabilization formulation does not demand the control parameters.

The rest of this work is organized as follows: In the next section, we define the boundary-value problem of linear elasticity and formulate the meshfree Galerkin method using the meshfree convex approximation. In Sect. 3, we present a stabilized meshfree Galerkin formulation based on an enhanced strain field induced by a displacement smoothing for the nodal integration method. Given a decomposed smoothed displacement field, a strain gradient stabilization that contains a tensor form of position-dependent stabilization parameter is derived. The corresponding discrete equations are given in Sect. 4. Same section discusses the preservation of linear exactness of the Galerkin approximation using the stabilization formulation. Several numerical examples are presented in Sect. 5 to illustrate the robustness and accuracy of the method. Final remarks are drawn in Sect. 6.

2 Preliminaries

In this section we consider the static response of an elastic body under plain strain condition. We assume the domain $\Omega \subset \mathbb{R}^2$ to be a bounded polygon with the smooth boundary $\Gamma = \partial\Omega$. Also, let \mathbf{u} be the displacement and further assume that the Dirichlet boundary conditions are applied on Γ_D and the Neumann boundary conditions are prescribed on Γ_N . For a prescribed body force $\mathbf{f}(X) \in L^2(\Omega)$, the governing equilibrium equation and boundary conditions are written as

$$\begin{aligned} -\nabla \cdot \boldsymbol{\sigma}(\mathbf{u}) &= \mathbf{f} \quad \text{in } \Omega \\ \mathbf{u} &= \mathbf{g} \quad \text{on } \Gamma_D \\ \boldsymbol{\sigma} \cdot \mathbf{n} &= \mathbf{t} \quad \text{on } \Gamma_N \end{aligned} \quad (\Gamma_D \cup \Gamma_N = \Gamma; \Gamma_D \cap \Gamma_N = \emptyset) \quad (1)$$

where \mathbf{g} is the prescribed displacement on Γ_D , \mathbf{t} is the prescribed traction, \mathbf{n} is the outward unit normal to the boundary Γ_N , and $\nabla \cdot$ stands for the divergence operator. The infinitesimal strain tensor $\boldsymbol{\varepsilon}(\mathbf{u})$ is defined by

$$\boldsymbol{\varepsilon}(\mathbf{u}) = \frac{1}{2} (\nabla \mathbf{u} + \mathbf{u} \nabla) \equiv \nabla^s \mathbf{u} \quad (2)$$

where ∇ is the gradient operator. In the case of linear isotropic elasticity, the Cauchy stress tensor $\boldsymbol{\sigma}$ and strain tensor $\boldsymbol{\varepsilon}$ have the following relationship

$$\boldsymbol{\sigma} = \mathbf{C} : \boldsymbol{\varepsilon}(\mathbf{u}) = 2\mu\boldsymbol{\varepsilon}(\mathbf{u}) + \lambda \operatorname{tr}(\boldsymbol{\varepsilon}(\mathbf{u}))\mathbf{I} \tag{3}$$

where \mathbf{C} is the elasticity tensor and \mathbf{I} is the identity tensor. The positive constants μ and λ the Lamé constants such that $\mu \in [\mu_1, \mu_2]$ with $0 < \mu_1 < \mu_2$ and $\lambda \in (0, \infty)$. The Lamé constants can be related to the Young’s modulus E and Poisson ratio ν by

$$\mu = \frac{E}{2(1+\nu)}, \quad \lambda = \frac{\nu E}{(1+\nu)(1-2\nu)} \tag{4}$$

The variational form of this problem is to find the displacement $\mathbf{u} \in \mathbf{V}^g = \{\mathbf{v} \in \mathbf{H}^1(\Omega) : \mathbf{v} = \mathbf{g} \text{ on } \Gamma_D\}$ such that for all $\delta\mathbf{u} \in \mathbf{V}$

$$\int_{\Omega} \delta(\nabla^s \mathbf{u}) : \mathbf{C} : (\nabla^s \mathbf{u}) \, d\Omega - \int_{\Omega} \delta\mathbf{u} \cdot \mathbf{f} \, d\Omega - \int_{\Gamma_N} \delta\mathbf{u} \cdot \mathbf{t} \, d\Gamma = 0 \tag{5}$$

where the space $\mathbf{V} = \mathbf{H}_0^1(\Omega)$ consists of functions in Sobolev space $\mathbf{H}^1(\Omega)$ which vanishes on the boundary in the sense of traces and is defined by

$$\mathbf{V}(\Omega) = \{\mathbf{v} : \mathbf{v} \in \mathbf{H}^1, \mathbf{v} = \mathbf{0} \text{ on } \Gamma_D\} \tag{6}$$

By the Lax–Milgram theorem [5], there exists a unique solution $\mathbf{u} \in \mathbf{V}^g$ to the problem. For simplicity, we assume the homogenous Dirichlet boundary conditions in the following derivation. The standard meshfree Galerkin method [3, 6, 26] is then formulated on a finite dimensional subspace $\mathbf{V}^h \subset \mathbf{V}$ employing the variational formulation of Eq. (5) to find $\mathbf{u}^h \in \mathbf{V}^h$ such that

$$\delta\Pi = \int_{\Omega} \delta(\nabla^s \mathbf{u}^h) : \mathbf{C} : (\nabla^s \mathbf{u}^h) \, d\Omega - \int_{\Omega} \delta\mathbf{u}^h \cdot \mathbf{f} \, d\Omega - \int_{\Gamma_N} \delta\mathbf{u}^h \cdot \mathbf{t} \, d\Gamma = 0 \quad \forall \delta\mathbf{u}^h \in \mathbf{V}^h \tag{7}$$

For a particle distribution noted by an index set $Z_I = \{\mathbf{X}_I\}_{I=1}^{NP}$, we approximate the displacement field using the meshfree approximation constructed by either conventional meshfree approximation methods or convex approximation methods [37] to give

$$\mathbf{u}^h(\mathbf{X}) = \sum_{I=1}^{NP} \Psi_I(\mathbf{X}) \tilde{\mathbf{u}}_I \equiv \hat{\mathbf{u}}(\mathbf{X}) \quad \forall \mathbf{X} \in \Omega \tag{8}$$

where NP is the total number of particles in discretization, and $\Psi_I(\mathbf{X})$, $I = 1, \dots, NP$ can be considered as the shape functions of the meshfree approximation for displacement field $\mathbf{u}^h(\mathbf{X})$. With the meshfree shape functions, we can define the corresponding finite-dimensional approximation

space to be $\mathbf{V}^h = \operatorname{span}\{\Psi_I(\mathbf{X}) : I \in Z_I \text{ and } \mathbf{X} \in \Omega\}$. In general, $\tilde{\mathbf{u}}_I$ is not the particle displacement and is often referred to as the “generalized displacement” [6] of particle I in meshfree Galerkin method. Using Eq. (8), the particle displacement at particle I can be expressed by

$$\mathbf{u}^h(\mathbf{X}_I) = \sum_{J=1}^{NP} \Psi_J(\mathbf{X}_I) \tilde{\mathbf{u}}_J \equiv \hat{\mathbf{u}}_I \tag{9}$$

where $\mathbf{X}_I = (X_I, Y_I)$ is the nodal coordinate of particle I . If the meshfree shape functions $\Psi_I(\mathbf{X})$ are constructed using a convex approximation, then they have the Kronecker-delta property on the boundary, i.e. $\hat{\mathbf{u}}_I = \tilde{\mathbf{u}}_I$ for $\forall \mathbf{X}_I \in \Gamma$. In this study, the first-order convex approximation is constructed by the GMF method [37] using the inverse tangent basis function and the cubic spline window function with a circular support. Giving a convex hull $\operatorname{Convex}(Z_I)$ of the node set $Z_I = \{\mathbf{X}_I, I = 1, \dots, NP\} \subset \mathbb{R}^2$ defined by

$$\begin{aligned} \operatorname{Convex}(Z_I) &= \left\{ \sum_{I=1}^{NP} \alpha_I \mathbf{X}_I \mid \alpha_I \in \mathbb{R}, \sum_{I=1}^{NP} \alpha_I = 1, \alpha_I \geq 0, \mathbf{X}_I \in Z_I \right\} \end{aligned} \tag{10}$$

the GMF method is used to construct a convex approximation of a given (smooth) function $\mathbf{u}(\mathbf{X})$ in the form of Eq. (8) such that the shape function $\Psi_I : \operatorname{Convex}(Z_I) \rightarrow \Re$ satisfies the following linear polynomial reproduction property

$$\sum_{I=1}^{NP} \Psi_I(\mathbf{X}) \mathbf{X}_I = \mathbf{X} \quad \forall \mathbf{X} \in \operatorname{Convex}(Z_I) \tag{11}$$

With the meshfree convex approximation, we can also define a H_0^1 -conforming subspace for the approximation of displacement field to be $\mathbf{V}^h := \operatorname{span}\{\Psi_I | (\operatorname{supp} \Psi_I)^0 \subset \Omega, I \in Z_I\}$. An evaluation of weak form in Eq. (1) using meshfree approximation and a direct nodal integration scheme leads to the spurious low or zero-energy modes. This is a consequence of the fact that field variables and their derivatives are calculated at the same points such that an alternating field variable has a zero gradient at particles [34]. The almost vanishing first derivatives at the nodes result in a discrete weak form that does not adequately reflect the strain energy and its contribution to the stiffness matrix is severely underestimated [2]. Mathematically, a semi-positive definite formulation is posed on the weak form of Eq. (7) by the direct nodal integration method, and the coercivity of bilinear form in Eq. (7) is not guaranteed unless a stabilization term is included. Figure 1 illustrates a typical 1D oscillation solution obtained from the direct nodal (DN) integration scheme.

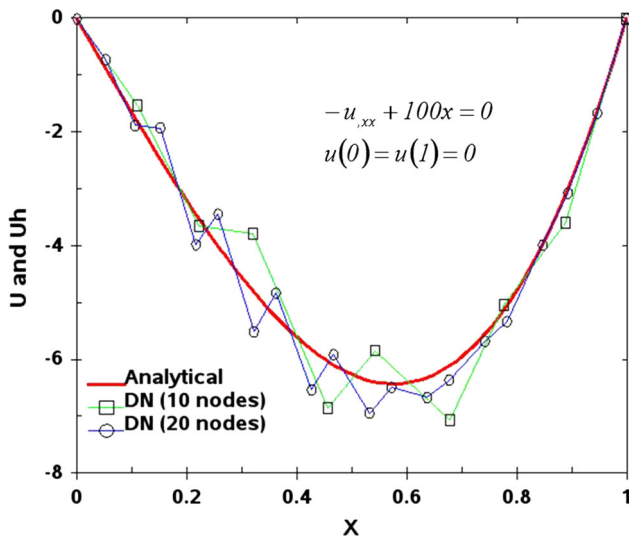


Fig. 1 Displacement oscillation in the direct nodal (DN) integration method for 1D problem

3 A stabilized meshfree nodal integration formulation for linear elasticity

3.1 A least-squares stabilization for meshfree Galerkin formulation

The GLS stabilization approach [2] presents a reconstructed weak form for meshfree nodal integration method in which a stabilization term consisting of the squares of the residual of the equilibrium equation is given as follows:

$$\begin{aligned} \delta\Pi &= \int_{\Omega} \delta\nabla^s(\mathbf{u}^h) : C\nabla^s(\mathbf{u}^h) d\Omega - \int_{\Omega} \delta\mathbf{u}^h \cdot \mathbf{f} d\Omega \\ &\quad - \int_{\Gamma_N} \delta\mathbf{u}^h \cdot \mathbf{t} d\Gamma + \frac{\alpha h^2}{E} \int_{\Omega} (\nabla \cdot \delta\boldsymbol{\sigma}(\mathbf{u}^h)) \\ &\quad \cdot (\nabla \cdot \boldsymbol{\sigma}(\mathbf{u}^h) + \mathbf{f}) \\ &= 0 \quad \forall \delta\mathbf{u}^h \in \mathbf{V}^h \end{aligned} \tag{12}$$

where α is the dimensionless stabilization control parameter, h is a characteristic length scale of the discretization. The divergence of the stress tensor in Eq. (12) can be expressed by

$$\nabla \cdot \boldsymbol{\sigma}(\mathbf{u}^h) = \nabla \cdot (C\boldsymbol{\varepsilon}(\mathbf{u}^h)) = C'\widehat{\boldsymbol{\varepsilon}}(\mathbf{u}^h) \tag{13}$$

where the notation $\widehat{\boldsymbol{\varepsilon}}$ represents the gradient of the strain measure and is expressed in the following matrix form

$$\widehat{\boldsymbol{\varepsilon}}(\mathbf{u}^h) = \begin{Bmatrix} u_{X,XX}^h \\ u_{X,XY}^h \\ u_{X,YY}^h \\ u_{Y,XX}^h \\ u_{Y,XY}^h \\ u_{Y,YY}^h \end{Bmatrix} \tag{14}$$

C' is a modified elasticity tensor from the matrix operation in Eq. (13) and its expression can be found explicitly in [2]. Rearranging Eq. (12) using Eq. (13) yields

$$\begin{aligned} \delta\Pi &= \int_{\Omega} \delta\boldsymbol{\varepsilon}(\mathbf{u}^h) : C\boldsymbol{\varepsilon}(\mathbf{u}^h) d\Omega - \int_{\Omega} \delta\mathbf{u}^h \cdot \mathbf{f} d\Omega \\ &\quad - \int_{\Gamma_N} \delta\mathbf{u}^h \cdot \mathbf{t} d\Gamma \\ &\quad + \frac{\alpha h^2}{E} \int_{\Omega} \delta(\widehat{\boldsymbol{\varepsilon}}(\mathbf{u}^h)) : (C'^T C')(\widehat{\boldsymbol{\varepsilon}}(\mathbf{u}^h)) \\ &\quad + \frac{\alpha h^2}{E} \int_{\Omega} \delta(C'\widehat{\boldsymbol{\varepsilon}}(\mathbf{u}^h) \cdot \mathbf{f}) = 0 \quad \forall \delta\mathbf{u}^h \in \mathbf{V}^h \end{aligned} \tag{15}$$

Since the term $\widehat{\boldsymbol{\varepsilon}}(\mathbf{u}^h)$ contains the gradients of the strain, the stabilization term in Eq. (15) can be considered as a term penalizing the jump of strain gradients at nodes that gives the control of the solution stabilization in meshfree nodal integration method. The idea of addition of a term penalizing the jump of strain gradients to the standard Galerkin formulation is not new. This stabilization approach was originally developed in the Streamline-upwind/Petro-Galerkin (SUPG) method [19] by appending residuals of the Euler-Lagrangian equations to the standard Galerkin variational equation for the advection-diffusion problems. Later on in the GLS method [20], the residuals of the Euler-Lagrangian equations were replaced by a least-squares form and led to a mesh-dependent term to enhance the coercivity of the formulation and recover the optimal rate of convergence for the displacement (or velocity)/pressure pairs. Nowadays, this stabilization technique has been widely used to stabilize the solutions of transport, acoustic waves and Stokes problems [4, 14, 32, 41].

To connect the stabilization term with an enhanced strain field in our formulation, Eq. (15) can be further written by

$$\begin{aligned} \delta\Pi &= \int_{\Omega} \delta\boldsymbol{\varepsilon}(\mathbf{u}^h) : C\boldsymbol{\varepsilon}(\mathbf{u}^h) d\Omega \\ &\quad - \int_{\Omega} \delta\mathbf{u}^h \cdot \mathbf{f} d\Omega - \int_{\Gamma_N} \delta\mathbf{u}^h \cdot \mathbf{t} d\Gamma \\ &\quad + \int_{\Omega} \delta(\widehat{\boldsymbol{\varepsilon}}(\mathbf{u}^h) - \boldsymbol{\varepsilon}(\mathbf{u}^h)) : (C'^T C')(\widehat{\boldsymbol{\varepsilon}}(\mathbf{u}^h) \\ &\quad - \boldsymbol{\varepsilon}(\mathbf{u}^h)) + \int_{\Omega} \delta(C'(\widehat{\boldsymbol{\varepsilon}}(\mathbf{u}^h) - \boldsymbol{\varepsilon}(\mathbf{u}^h)) \cdot \mathbf{f}) \\ &= 0 \quad \forall \delta\mathbf{u}^h \in \mathbf{V}^h \end{aligned} \tag{16}$$

where $\bar{\boldsymbol{\varepsilon}}$ can be regarded as a stabilized strain field defined by

$$\bar{\boldsymbol{\varepsilon}}(\mathbf{u}^h) = \boldsymbol{\varepsilon}(\mathbf{u}^h) + \alpha_s \widehat{\boldsymbol{\varepsilon}}(\mathbf{u}^h) \tag{17}$$

in which $\alpha_s = h\sqrt{\frac{\alpha}{E}}$ denotes a length scale dependent stabilization parameter. The term $\alpha_s \widehat{\boldsymbol{\varepsilon}}(\mathbf{u}^h)$ in Eq. (17) can be realized as an enhanced strain for stabilization. This strain gradients penalization allows the formulation to stabilize the solution of direct nodal integration method and provides the possibility to recover the optimal rate of convergence in meshfree Galerkin framework [2]. Nevertheless, the optimal choice of stabilization control parameter α_s remains an open question. From our numerical experiences, the selection of stabilization control parameter α_s is usually related to the nodal support sizes. We also found out that the choice of stabilization parameter is sensitive to the irregularity of nodal distribution in meshfree discretization. Generally, a proper stabilization control parameter needs to be calibrated problem by problem in the engineering practice. This may be one of the reasons that GLS stabilization approach has not gained universal popularity in meshfree community for the solid and structure analyses.

3.2 An enhanced strain from the decomposed smoothed displacement field

In this study, an alternative strain gradient penalization approach is developed through an enhanced strain introduced by a decomposed smoothed displacement field. We first consider a Taylor series expansion of a function $\hat{\mathbf{u}}(\mathbf{Y})$ about a point $\mathbf{Y} = \mathbf{X}$ to be

$$\begin{aligned} \hat{\mathbf{u}}(\mathbf{Y}) &= \hat{\mathbf{u}}(\mathbf{X}) + \nabla \hat{\mathbf{u}}(\mathbf{X}) \cdot (\mathbf{Y} - \mathbf{X}) \\ &+ \frac{1}{2!} \nabla^{(2)} \hat{\mathbf{u}}(\mathbf{X}) \cdot^{(2)} (\mathbf{Y} - \mathbf{X})^{(2)} \\ &+ \frac{1}{3!} \nabla^{(3)} \hat{\mathbf{u}}(\mathbf{X}) \cdot^{(3)} (\mathbf{Y} - \mathbf{X})^{(3)} + \dots \end{aligned} \tag{18}$$

where $\nabla^{(n)}$ denotes the n th order gradient operator and $\cdot^{(n)}$ denotes the n th order inner product.

A smoothing of displacement field is first devised and is defined by [42]

$$\bar{\mathbf{u}}(\mathbf{X}) \stackrel{def.}{=} \int_{\Omega} \tilde{\Psi}(\mathbf{Y}; \mathbf{X}) \hat{\mathbf{u}}(\mathbf{Y}) d\Omega \tag{19}$$

where \mathbf{Y} denotes the position of the infinitesimal volume $d\Omega$, $\hat{\mathbf{u}}(\mathbf{Y})$ is an oscillatory displacement field at position \mathbf{Y} produced by the direct nodal integration method, and $\tilde{\Psi}$ is the displacement smoothing function. Using the assumption that displacement smoothing function is continuous in Ω , the corresponding stabilized strain field can be expressed by

$$\bar{\boldsymbol{\varepsilon}}(\mathbf{u}) \equiv \Theta(\boldsymbol{\varepsilon}(\mathbf{u})) = \nabla_X \bar{\mathbf{u}}(\mathbf{X}) = \int_{\Omega} \nabla_X \tilde{\Psi}(\mathbf{Y}; \mathbf{X}) \hat{\mathbf{u}}(\mathbf{Y}) d\Omega \tag{20}$$

where $\Theta : L^2(\Omega) \rightarrow L^2(\Omega)$ denotes a L_2 projection operator. It is assumed that the displacement smoothing functions $\tilde{\Psi}$ are also constructed by the meshfree convex approximation and satisfy the linear polynomial reproduction condition. In another words, the smoothed displacement field $\bar{\mathbf{u}}(\mathbf{X})$ defined in Eq. (19) equals to $\hat{\mathbf{u}}(\mathbf{X})$ for homogeneous displacement states. The symbol $(\boldsymbol{\xi})^{(n)}$ designates the n factor dyadic product $(\boldsymbol{\xi})(\boldsymbol{\xi}) \cdots (\boldsymbol{\xi})$ for vector $\boldsymbol{\xi}$. Substituting Eq. (18) into Eq. (19) and truncating the Taylor series after the quadratic term together with a use of the linear polynomial reproduction condition of $\tilde{\Psi}$ lead to the following smoothed displacement field approximated in terms of unsmoothed displacement and its gradients

$$\begin{aligned} \bar{\mathbf{u}}(\mathbf{X}) &\approx \int_{\Omega} \tilde{\Psi}(\mathbf{Y}; \mathbf{X}) \hat{\mathbf{u}}(\mathbf{X}) d\Omega \\ &+ \int_{\Omega} \tilde{\Psi}(\mathbf{Y}; \mathbf{X}) \nabla \hat{\mathbf{u}}(\mathbf{X}) (\mathbf{Y} - \mathbf{X}) d\Omega \\ &+ \frac{1}{2!} \int_{\Omega} \tilde{\Psi}(\mathbf{Y}; \mathbf{X}) \nabla^{(2)} \hat{\mathbf{u}}(\mathbf{X}) \cdot^{(2)} (\mathbf{Y} - \mathbf{X})^{(2)} d\Omega \\ &= \hat{\mathbf{u}}(\mathbf{X}) \int_{\Omega} \tilde{\Psi}(\mathbf{Y}; \mathbf{X}) d\Omega \\ &+ \nabla \hat{\mathbf{u}}(\mathbf{X}) \underbrace{\left(\int_{\Omega} \tilde{\Psi}(\mathbf{Y}; \mathbf{X}) (\mathbf{Y}) d\Omega - \mathbf{X} \int_{\Omega} \tilde{\Psi}(\mathbf{Y}; \mathbf{X}) d\Omega \right)}_{=0} \\ &+ \nabla^{(2)} \hat{\mathbf{u}}(\mathbf{X}) \cdot^{(2)} \left(\frac{1}{2!} \int_{\Omega} \tilde{\Psi}(\mathbf{Y}; \mathbf{X}) (\mathbf{Y} - \mathbf{X})^{(2)} d\Omega \right) \\ &= \hat{\mathbf{u}}(\mathbf{X}) \int_{\Omega} \tilde{\Psi}(\mathbf{Y}; \mathbf{X}) d\Omega \\ &+ \nabla^{(2)} \hat{\mathbf{u}}(\mathbf{X}) \cdot^{(2)} \left(\frac{1}{2!} \int_{\Omega} \tilde{\Psi}(\mathbf{Y}; \mathbf{X}) (\mathbf{Y} - \mathbf{X})^{(2)} d\Omega \right) \\ &= \hat{\mathbf{u}}(\mathbf{X}) + \nabla^{(2)} \hat{\mathbf{u}}(\mathbf{X}) \cdot^{(2)} \boldsymbol{\eta}(\mathbf{X}) \\ &= \hat{\mathbf{u}}(\mathbf{X}) + \tilde{\mathbf{u}}(\hat{\mathbf{u}}(\mathbf{X})) \end{aligned} \tag{21}$$

where

$$\boldsymbol{\eta}(\mathbf{X}) = \frac{1}{2!} \int_{\Omega} \tilde{\Psi}(\mathbf{Y}; \mathbf{X}) (\mathbf{Y} - \mathbf{X})^{(2)} d\Omega \tag{22}$$

defines the tensor form of position dependent coefficients and $\tilde{\mathbf{u}} = \nabla^{(2)} \hat{\mathbf{u}} \cdot^{(2)} \boldsymbol{\eta}$ denotes the decomposed smoothed displacement field or enhanced displacement field introduced for providing the stabilization effect in the meshfree nodal integration method.

In the direct nodal integration method, the discrete form of Eq. (21) can be expressed by

$$\begin{aligned} \bar{\mathbf{u}}(\mathbf{X}_I) &= \hat{\mathbf{u}}(\mathbf{X}_I) + \nabla^{(2)}\hat{\mathbf{u}}(\mathbf{X}_I) \cdot^{(2)} \boldsymbol{\eta}(\mathbf{X}_I) \\ &= \hat{\mathbf{u}}(\mathbf{X}_I) + \tilde{\mathbf{u}}(\mathbf{X}_I) \quad \forall \mathbf{X}_I \in \Omega \end{aligned} \tag{23}$$

in which $|\boldsymbol{\eta}(\mathbf{X}_I)| \propto h^2$ is proportional to a length squared. With the meshfree convex approximations defined in Eq. (11) for the displacement smoothing functions $\tilde{\Psi}$, the position dependent coefficients $\boldsymbol{\eta}(\mathbf{X}_I)$ can be shown to vanish on the global boundary Γ

$$\boldsymbol{\eta}(\mathbf{X}_I) = \mathbf{0} \quad \forall \mathbf{X}_I \in \Gamma \tag{24}$$

In other words, the discrete enhanced displacement field satisfies $\tilde{\mathbf{u}}(\mathbf{X}_I) = \mathbf{0} \quad \forall \mathbf{X}_I \in \Gamma$. Therefore the Dirichlet boundary condition is satisfied *ab initio* by the enhanced displacement field $\tilde{\mathbf{u}}$.

In essence, the stabilized strain field defined in Eq. (19) is different from the non-local strain used in the regularization of strain localization problem [7,41]. Their difference can be easily identified by the following analysis in the case of uniform discretization. Given a “boundary region” $B(G_I)$ of a node set $G_I = \{\mathbf{X}_I, I = 1, \dots, MP\} \subset R^2$ defined by

$$B(G_I) := \{\mathbf{X}_I \in G_I, \text{supp}(\mathbf{X}_I) \cap \Gamma \neq \emptyset\} \tag{25}$$

the direct nodal integration of Eq. (19) gives

$$\begin{aligned} \bar{\boldsymbol{\varepsilon}}(\mathbf{X}) &\equiv \Theta_h \boldsymbol{\varepsilon}(\mathbf{X}) = \int_{\Omega} \nabla_X \tilde{\Psi}(\mathbf{Y}; \mathbf{X}) \mathbf{u}^h(\mathbf{Y}) d\Omega \\ &= \int_{\Omega/B} \nabla_X \tilde{\Psi}(\mathbf{Y}; \mathbf{X}) \mathbf{u}^h(\mathbf{Y}) d\Omega \\ &\quad + \int_B \nabla_X \tilde{\Psi}(\mathbf{Y}; \mathbf{X}) \mathbf{u}^h(\mathbf{Y}) d\Omega \end{aligned} \tag{26}$$

where Θ_h is the discrete analogue of Θ . In uniform nodal distribution, the term $\int_{\Omega/B} \nabla_X \tilde{\Psi}(\mathbf{Y}; \mathbf{X}) \mathbf{u}^h(\mathbf{Y}) d\Omega$ in Eq. (26) has the following property

$$\nabla_X \tilde{\Psi}(\mathbf{Y}; \mathbf{X}) = -\nabla_Y \tilde{\Psi}(\mathbf{Y}; \mathbf{X}) \tag{27}$$

The combination of Eqs. (26) and (27) with a use of divergence theorem give

$$\begin{aligned} \bar{\boldsymbol{\varepsilon}}(\mathbf{X}) &= - \int_{\Omega/B} \nabla_Y \tilde{\Psi}(\mathbf{Y}; \mathbf{X}) \mathbf{u}^h(\mathbf{Y}) d\Omega \\ &\quad + \int_B \nabla_X \tilde{\Psi}(\mathbf{Y}; \mathbf{X}) \mathbf{u}^h(\mathbf{Y}) d\Omega \\ &= - \int_{\Omega/B} \nabla_Y \tilde{\Psi}(\mathbf{Y}; \mathbf{X}) \mathbf{u}^h(\mathbf{Y}) d\Omega \\ &\quad + \int_B \nabla_X \tilde{\Psi}(\mathbf{Y}; \mathbf{X}) \mathbf{u}^h(\mathbf{Y}) d\Omega \\ &\quad + \underbrace{\left(- \int_B \nabla_Y \tilde{\Psi}(\mathbf{Y}; \mathbf{X}) \mathbf{u}^h(\mathbf{Y}) d\Omega + \int_B \nabla_Y \tilde{\Psi}(\mathbf{Y}; \mathbf{X}) \mathbf{u}^h(\mathbf{Y}) d\Omega \right)}_{=0} \end{aligned}$$

$$\begin{aligned} &= - \int_{\Omega} \nabla_Y \tilde{\Psi}(\mathbf{Y}; \mathbf{X}) \mathbf{u}^h(\mathbf{Y}) d\Omega \\ &\quad + \int_B \left(\nabla_X \tilde{\Psi}(\mathbf{Y}; \mathbf{X}) + \nabla_Y \tilde{\Psi}(\mathbf{Y}; \mathbf{X}) \right) \mathbf{u}^h(\mathbf{Y}) d\Omega \\ &= \int_{\Omega} \tilde{\Psi}(\mathbf{Y}; \mathbf{X}) \nabla_Y \mathbf{u}^h(\mathbf{Y}) d\Omega - \int_{\Gamma} \tilde{\Psi}(\mathbf{Y}; \mathbf{X}) \mathbf{n} \cdot \mathbf{u}^h d\Gamma \\ &\quad + \int_B \left(\nabla_X \tilde{\Psi}(\mathbf{Y}; \mathbf{X}) + \nabla_Y \tilde{\Psi}(\mathbf{Y}; \mathbf{X}) \right) \mathbf{u}^h(\mathbf{Y}) d\Omega \\ &= \tilde{\boldsymbol{\varepsilon}}(\mathbf{X}) + \bar{\boldsymbol{\varepsilon}}(\mathbf{X}) \end{aligned} \tag{28}$$

where $\tilde{\boldsymbol{\varepsilon}}(\mathbf{X})$ is the standard expression of non-local strain in the regularization of strain localization problem [7] and it is defined by

$$\tilde{\boldsymbol{\varepsilon}}(\mathbf{X}) \equiv \int_{\Omega} \tilde{\Psi}(\mathbf{Y}; \mathbf{X}) \boldsymbol{\varepsilon}^h(\mathbf{Y}) d\Omega \tag{29}$$

Now the difference between the present stabilized strain $\bar{\boldsymbol{\varepsilon}}(\mathbf{X})$ and the non-local strain $\tilde{\boldsymbol{\varepsilon}}(\mathbf{X})$ can be expressed by

$$\begin{aligned} \bar{\boldsymbol{\varepsilon}}(\mathbf{X}) &\equiv \bar{\boldsymbol{\varepsilon}}(\mathbf{X}) - \tilde{\boldsymbol{\varepsilon}}(\mathbf{X}) \\ &= \int_B \left(\nabla_X \tilde{\Psi}(\mathbf{Y}; \mathbf{X}) + \nabla_Y \tilde{\Psi}(\mathbf{Y}; \mathbf{X}) \right) \mathbf{u}^h(\mathbf{Y}) d\Omega \\ &\quad - \int_{\Gamma} \tilde{\Psi}(\mathbf{Y}; \mathbf{X}) \mathbf{n} \cdot \mathbf{u}^h d\Gamma \end{aligned} \tag{30}$$

In our numerical implementation, a modification of discrete stabilized strain field is obtained from the decomposed displacement field in Eq. (23) with a neglect of derivative terms after second-order in the displacement such that

$$\bar{\Theta}_h \boldsymbol{\varepsilon}(\hat{\mathbf{u}}) = \boldsymbol{\varepsilon}(\hat{\mathbf{u}}) + \nabla \tilde{\mathbf{u}}(\hat{\mathbf{u}}) \approx \nabla \hat{\mathbf{u}} + \bar{\nabla}^{(2)} \hat{\mathbf{u}} \tag{31}$$

where $\bar{\Theta}_h$ is a modified discrete smoothed strain operator, $\bar{\nabla}^{(2)}$ denotes a kind of second-order gradient operator, and $\bar{\nabla}^{(2)} \hat{\mathbf{u}} \approx \nabla \tilde{\mathbf{u}}(\hat{\mathbf{u}})$ corresponds to an approximated enhanced strain field for stabilization that contains only the second-order derivatives of displacements and has the following explicit form

$$\bar{\nabla}^{(2)} \hat{\mathbf{u}} = \frac{1}{2} \left(\nabla \boldsymbol{\eta} : \hat{\mathbf{u}} \nabla^{(2)} + \left(\nabla \boldsymbol{\eta} : \hat{\mathbf{u}} \nabla^{(2)} \right)^T \right) \tag{32}$$

The index forms of Eq. (32) in multi-dimensions are given by

$$\left[\bar{\nabla}^{(2)} \hat{\mathbf{u}} \right]_{ij} = \frac{1}{2} \left(\eta_{kl,i} \hat{u}_{m,nj} \delta_{lm} \delta_{kn} + \hat{u}_{k,li} \eta_{mn,j} \delta_{km} \delta_{ln} \right) \tag{33}$$

or

$$\begin{aligned} \left[\bar{\nabla}^{(2)} \hat{\mathbf{u}} \right]_{ij} &= \frac{1}{2} \left(\sum_{k=1}^3 \sum_{l=1}^3 \frac{\partial \eta_{kl}}{\partial X_i} \frac{\partial^2 \hat{u}_l}{\partial X_k \partial X_j} + \sum_{k=1}^3 \sum_{l=1}^3 \frac{\partial^2 \hat{u}_l}{\partial X_i \partial X_k} \frac{\partial \eta_{lk}}{\partial X_j} \right) \end{aligned} \tag{34}$$

Eq. (33) will be used in this study for the two-dimensional linear elastic analysis. The corresponding displacement gradient matrices using Eq. (33) for the stabilization computation are given in the next section.

To introduce the enhanced strain field in Eq. (31) into the standard variational formulation, the penalty approach is considered:

$$\bar{\Pi} = \arg \min_{\mathbf{v} \in \mathbf{H}^1(\Omega)} \left[\Pi(\mathbf{v}) + \frac{1}{2} \int_{\Omega} (\bar{\Theta}_h \boldsymbol{\varepsilon}(\mathbf{v}) - \boldsymbol{\varepsilon}(\mathbf{v})) : \mathbf{C} : (\bar{\Theta}_h \boldsymbol{\varepsilon}(\mathbf{v}) - \boldsymbol{\varepsilon}(\mathbf{v})) d\Omega \right] \tag{35}$$

With the enhanced strain field defined in Eq. (31), the minimization problem of (35) leads to the following stabilized discrete weak form by the nodal integration method: finding $\hat{\mathbf{u}} \in \mathbf{V}^h$, such that

$$a^h(\hat{\mathbf{u}}, \delta \hat{\mathbf{u}}) = l(\delta \hat{\mathbf{u}}) \quad \forall \delta \hat{\mathbf{u}} \in \mathbf{V}^h \tag{36}$$

where

$$\begin{aligned} a^h(\hat{\mathbf{u}}, \delta \hat{\mathbf{u}}) &= \int_{\Omega} \delta (\nabla^s \hat{\mathbf{u}}) : \mathbf{C} : (\nabla^s \hat{\mathbf{u}}) d\Omega \\ &\quad + \int_{\Omega} \delta (\bar{\nabla}^{(2)} \hat{\mathbf{u}}) : \mathbf{C} : (\bar{\nabla}^{(2)} \hat{\mathbf{u}}) d\Omega \\ &= a_{stan}^h(\hat{\mathbf{u}}, \delta \hat{\mathbf{u}}) + a_{stab}^h(\hat{\mathbf{u}}, \delta \hat{\mathbf{u}}) \end{aligned} \tag{37}$$

$$l(\delta \hat{\mathbf{u}}) = \int_{\Omega} \delta \hat{\mathbf{u}} \cdot \mathbf{f} d\Omega + \int_{\Gamma_N} \delta \hat{\mathbf{u}} \cdot \mathbf{t} d\Gamma \tag{38}$$

The notation a_{stan}^h in Eq. (37) denotes the standard bilinear form. The stabilized bilinear form a_{stab}^h is given by

$$\begin{aligned} a_{stab}^h(\hat{\mathbf{u}}, \delta \hat{\mathbf{u}}) &= \int_{\Omega} \delta (\bar{\Theta}_h \boldsymbol{\varepsilon}(\hat{\mathbf{u}}) - \boldsymbol{\varepsilon}(\hat{\mathbf{u}})) : \mathbf{C} : (\bar{\Theta}_h \boldsymbol{\varepsilon}(\hat{\mathbf{u}}) - \boldsymbol{\varepsilon}(\hat{\mathbf{u}})) d\Omega \\ &= \int_{\Omega} \delta (\bar{\nabla}^{(2)} \hat{\mathbf{u}}) : \mathbf{C} : (\bar{\nabla}^{(2)} \hat{\mathbf{u}}) d\Omega \end{aligned} \tag{39}$$

which corresponds to the variation of stabilized potential energy. Apparently, the bilinear term $a_{stab}^h(\cdot, \cdot)$ is symmetric, continuous and non-negative. Now the modified bilinear form a^h is coercive with respect to a broken energy norm defined by

$$\| |\mathbf{v}^h| \|^2 = |\mathbf{v}^h|_1^2 + a_{stab}^h(\mathbf{v}^h, \mathbf{v}^h) \quad \forall \mathbf{v}^h \in \mathbf{V}^h \tag{40}$$

where $|\cdot|_1$ stands for the semi-norm by standard notation in the Sobolev space. The penalty error in Eq. (40) stems from

the application of direct nodal integration scheme to the stabilized term and can be shown by

$$\begin{aligned} a^h(\mathbf{u} - \mathbf{u}^h, \mathbf{v}^h) &= a^h(\mathbf{u}, \mathbf{v}^h) - l(\mathbf{v}^h) = a_{stab}^h(\mathbf{u}, \mathbf{v}^h) \\ &= \int_{\Omega} (\bar{\nabla}^{(2)} \mathbf{u}) : \mathbf{C} : (\bar{\nabla}^{(2)} \mathbf{v}^h) d\Omega \\ &= \sum_{I=1}^{NP} (\bar{\nabla}^{(2)} \mathbf{u}(\mathbf{X}_I) : \mathbf{C} : \bar{\nabla}^{(2)} \mathbf{v}^h(\mathbf{X}_I)) V_I \quad \text{for } \mathbf{v}^h \in \mathbf{V}_h \end{aligned} \tag{41}$$

where V_I denotes the volume of node I . In other words, Eq. (41) can be used to measure the effect of $\mathbf{V}_h \not\subset \mathbf{V}$ in the penalty variational formulation setting. In Sect. 5, the discrete form of Eq. (41) will be employed to evaluate the penalty error of the present stabilization formulation for the numerical convergence study.

4 Discrete equations and preservation of constant stress field

The corresponding discrete equations of the present stabilization formulation for two-dimensional linear elastic analysis are summarized in the following

$$\bar{\mathbf{K}} \tilde{\mathbf{U}} = \mathbf{f}^{ext} \tag{42}$$

$$\bar{\mathbf{K}} = \mathbf{K} + \tilde{\mathbf{K}} \tag{43}$$

$$\mathbf{K}_{IJ} = \sum_{K=1}^{NP} \mathbf{B}_I^T(\mathbf{X}_K) \mathbf{C} \mathbf{B}_J(\mathbf{X}_K) V_K \tag{44}$$

$$\tilde{\mathbf{K}}_{IJ} = \sum_{K=1}^{NP} \tilde{\mathbf{B}}_I^T(\mathbf{X}_K) \mathbf{C} \tilde{\mathbf{B}}_J(\mathbf{X}_K) V_K \tag{45}$$

$$\mathbf{f}_I^{ext} = \sum_{K=1}^{NP} \Psi_I(\mathbf{X}_K) \mathbf{f}(\mathbf{X}_K) V_K + \sum_{K=1}^{NB} \Psi_I(\mathbf{X}_K) \mathbf{t}(\mathbf{X}_K) L_K \tag{46}$$

$$\tilde{\mathbf{B}}_I(\mathbf{X}) = \begin{bmatrix} \tilde{b}_{11} & \tilde{b}_{12} \\ \tilde{b}_{21} & \tilde{b}_{22} \\ \tilde{b}_{31} & \tilde{b}_{32} \end{bmatrix} \tag{47}$$

where the components in Eq. (47) are given in Appendix A. The vector $\tilde{\mathbf{U}} = [\tilde{\mathbf{u}}_1 \tilde{\mathbf{u}}_2 \cdots \tilde{\mathbf{u}}_{NP}]$ contains the problem unknowns for generalized nodal displacements. V_I denotes the volume of node I . NB denotes the number of boundary nodes and L_K is the length associated with the boundary node along the global boundary. \mathbf{B}_I is the standard displacement gradient matrix of node I obtained by the direct nodal integration scheme. Note the numerical evaluation of Eq. (42)

using the direct nodal integration scheme results in a symmetric linear system.

A practical numerical method in solid mechanics applications is often required to pass the patch test in which a constant stress field has to be reproduced exactly. It is ready to show that the present formulation will pass the constant stress patch test if the well-known SCNI scheme [9] is adopted for the computation of standard bilinear form in Eq. (37). The application of SCNI scheme to Eq. (37) leads to the following gradient-type stabilization for the SCNI formulation

$$\begin{aligned} \delta \bar{\Pi}(\hat{\mathbf{u}}, \tilde{\boldsymbol{\varepsilon}}) &= \int_{\Omega} \delta \tilde{\boldsymbol{\varepsilon}} : \mathbf{C} : \tilde{\boldsymbol{\varepsilon}} d\Omega \\ &+ \int_{\Omega} \delta \left(\bar{\nabla}^{(2)} \hat{\mathbf{u}} \right) : \mathbf{C} : \left(\bar{\nabla}^{(2)} \hat{\mathbf{u}} \right) d\Omega \\ &- \int_{\Omega} \delta \hat{\mathbf{u}} \cdot \mathbf{f} d\Omega - \int_{\Gamma_N} \delta \hat{\mathbf{u}} \cdot \mathbf{t} d\Gamma \end{aligned} \tag{48}$$

In two-dimensional problem, the smoothed strain $\tilde{\boldsymbol{\varepsilon}}$ in Eq. (48) is defined by Chen et al. [9] as:

$$\tilde{\boldsymbol{\varepsilon}}(\mathbf{X}_m) = \frac{1}{A_m} \int_{\Omega_m} \hat{\boldsymbol{\varepsilon}}(\hat{\mathbf{u}}(\mathbf{X})) \Phi_m(\mathbf{X}) d\Omega \tag{49}$$

where Ω_m is a representative domain of node m which can be constructed based on the Voronoi diagrams or finite element mesh in SCNI method. $A_m = \int_{\Omega_m} d\Omega$ is the associated area of Ω_m . $\Phi_m(\mathbf{X})$ is the characteristic or strain smoothing function of the nodal representative domain Ω_m defined by

$$\Phi_m(\mathbf{X}) = \begin{cases} 1, & \text{if } \mathbf{X} \in \Omega_m \\ 0, & \text{else} \end{cases} \tag{50}$$

We continue to show that the present strain gradient stabilization for SCNI formulation in Eq. (48) passes the constant stress patch test.

Proof First of all, let’s assume the exact solution for the two-dimensional linear displacement field in the patch test to be expressed by $\hat{\mathbf{u}}(\mathbf{X}_I) = \mathbf{X}_I, I = 1, \dots, NP$ in the nodal integration method. Using Eq. (23), the smoothed displacement field is approximated by

$$\begin{aligned} \bar{\mathbf{u}}(\mathbf{X}) &= \hat{\mathbf{u}}(\mathbf{X}) + \nabla^{(2)} \hat{\mathbf{u}}(\mathbf{X}) \cdot^{(2)} \boldsymbol{\eta}(\mathbf{X}) \\ &= \sum_{I=1}^{NP} \psi_I(\mathbf{X}) \hat{\mathbf{u}}(\mathbf{X}_I) + \left(\sum_{I=1}^{NP} \boldsymbol{\Xi}_I(\mathbf{X}) \right) \cdot^{(2)} \boldsymbol{\eta}(\mathbf{X}) \end{aligned} \tag{51}$$

where

$$\nabla^{(2)} \hat{\mathbf{u}}(\mathbf{X}) = \sum_{I=1}^{NP} \boldsymbol{\Xi}_I(\mathbf{X}) \tag{52}$$

Then using the linear reproducing property for displacement smoothing function in Eq. (18), we have

$$\begin{aligned} \sum_{I=1}^{NP} \boldsymbol{\Xi}_I(\mathbf{X}) &\approx \left[\sum_{I=1}^{NP} \left(\psi_{I,XX}(\mathbf{X}) \right. \right. \\ &\quad \left. \left. + \psi_{I,XY}(\mathbf{X}) \right) \hat{u}_X(\mathbf{X}_I) \sum_{I=1}^{NP} \left(\psi_{I,YX}(\mathbf{X}) \right. \right. \\ &\quad \left. \left. + \psi_{I,YY}(\mathbf{X}) \right) \hat{u}_Y(\mathbf{X}_I) \right] \\ &= [0 \ 0] \end{aligned} \tag{53}$$

where $\hat{\mathbf{u}}(\mathbf{X}_I) = [\hat{u}_X(\mathbf{X}_I) \ \hat{u}_Y(\mathbf{X}_I)]$. The combination of Eqs. (51) and (53) yields

$$\begin{aligned} \bar{\mathbf{u}}(\mathbf{X}_J) &= \sum_{I=1}^{NP} \psi_I(\mathbf{X}_J) \hat{\mathbf{u}}(\mathbf{X}_I) + \nabla^{(2)} \hat{\mathbf{u}}(\mathbf{X}_J) \cdot^{(2)} \boldsymbol{\eta}(\mathbf{X}_J) \\ &= \hat{\mathbf{u}}(\mathbf{X}_J) \quad \text{and} \quad \tilde{\mathbf{u}}(\mathbf{X}_J) = \mathbf{0} \quad \forall \mathbf{X}_J \in \Omega \end{aligned} \tag{54}$$

The results in Eq. (54) imply that the enhanced displacement field is null. In other words, we have

$$\nabla^{(2)} \hat{\mathbf{u}}(\mathbf{X}_J) = \mathbf{0} \quad \text{thus} \quad \bar{\nabla}^{(2)} \hat{\mathbf{u}}(\mathbf{X}_J) = \mathbf{0} \quad \forall \mathbf{X}_J \in \Omega \tag{55}$$

which implies that the present strain gradient stabilization for SCNI formulation in Eq. (48) reduces to the standard SCNI formulation [9] in the constant stress patch test. Hence, the proof follows. \square

5 Numerical examples

In this section, five benchmark examples are analyzed to study the performance of present stabilization method in linear elastic problems. Plain strain condition is assumed in two-dimensional problems. As comparison, we also provide the results using the direct nodal (DN) integration method and the standard SCNI method [9]. Unless otherwise specified, a normalized nodal support size of 2.0 is used for the direct nodal integration method and the standard SCNI method in the two-dimensional analyses. For the present method, the normalized nodal support size of 2.5 is considered for the two-dimensional problems. In all test cases, we have used the meshfree convex approximations [37] to simplify the boundary condition enforcement. To explore the concept of the method, we simply consider $\tilde{\psi}_I(\mathbf{X}) = \psi_I(\mathbf{X})$ in the numerical study. For results using the present stabilization formulation, the SCNI method is not applied to the standard bilinear term in the all numerical analyses. A dimensionless unit system is adopted in this paper for convenience. The errors of the discrete solutions are measured in a stress-error norm defined by

$$e_{u\sigma}^h \equiv \sqrt{\int_{\Omega} \left[(\sigma_{xx}^h - \sigma_{xx})^2 + (\sigma_{xy}^h - \sigma_{xy})^2 + (\sigma_{yy}^h - \sigma_{yy})^2 \right] d\Omega} \tag{56}$$

Since the numerical evaluation of broken energy norm error in Eq. (40) is difficult, an energy norm error associated with the stabilization term in Eq. (41) is defined in the following to investigate the convergence order of penalty error in the present method.

$$e_{ue}^h \equiv \frac{|a_{stab}^h(\mathbf{u}^h, \mathbf{u}^h)|}{\|\mathbf{u}^h\|_1} \tag{57}$$

Finally, all the deformation plots are illustrated with the help of background meshes for the demonstration purpose.

5.1 1D problem with third-order solution

This 1D example has been utilized previously in Sect. 2 for the illustration of solution oscillation problem in the direct nodal integration method. In this numerical example, the enhanced accuracy in the present method is studied and used to compare with that of direct nodal integration and standard SCNI methods. The model problem is defined by

$$-u_{,xx} + 100x = 0, \quad 0 \leq x \leq 1 \tag{58}$$

with boundary conditions

$$u(0) = u(1) = 0 \tag{59}$$

Two slightly irregular meshfree models containing 10- and 20-node with a normalized support size of 1.6 is used in the analysis. This normalized support size corresponds to an actual nodal support size of 0.178 and 0.084 for 10- and 20-node models, respectively. As reported previously in Fig. 1, the direct nodal integration method displays severe oscillations of the solution as shown in Fig. 2a, b for 10- and 20-node model, respectively. The solution oscillation in direct nodal integration method can be greatly improved by the standard SCNI method, although small oscillation is still visible in the SCNI solution particularly for the 10-node model. On the other hand, the present method produces very accurate solution and demonstrates its effectiveness in providing the stabilization effect.

5.2 Cantilever beam

A cantilever beam problem under plane strain condition, as shown in Fig. 3, is considered for the numerical study of

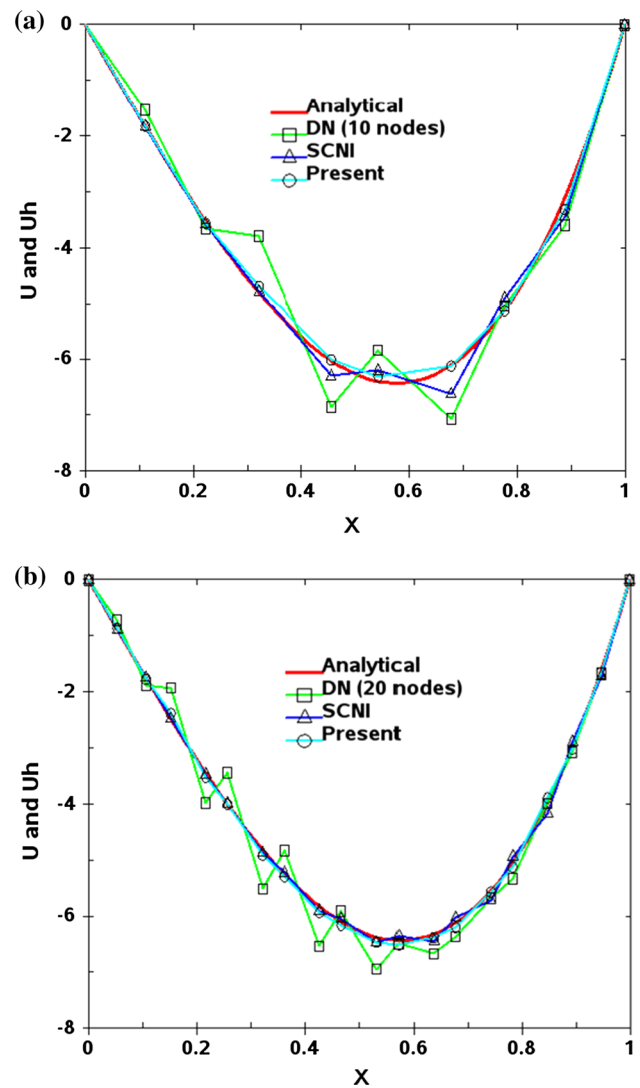


Fig. 2 Comparison of solution in 1D problem. a 10-node model, b 20-node model

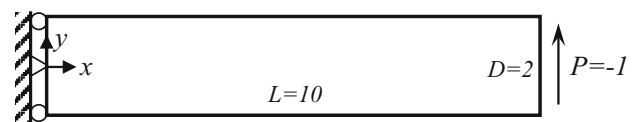


Fig. 3 Cantilever beam model

convergence properties in this two-dimensional linear analysis. Analytical displacement field is prescribed along $X = 0$, and parabolic vertical traction P is applied along $X = 10$. The analytical displacement and stress solutions of the problem are available in [33]. The material properties used in the analysis are: Young’s modulus $E = 1000$, Poisson ratio $\nu = 0.3$.

Figure 4a shows the convergence results in stress-error norms. Since the exact solution is relatively smooth and all three numerical methods do not produce any spurious

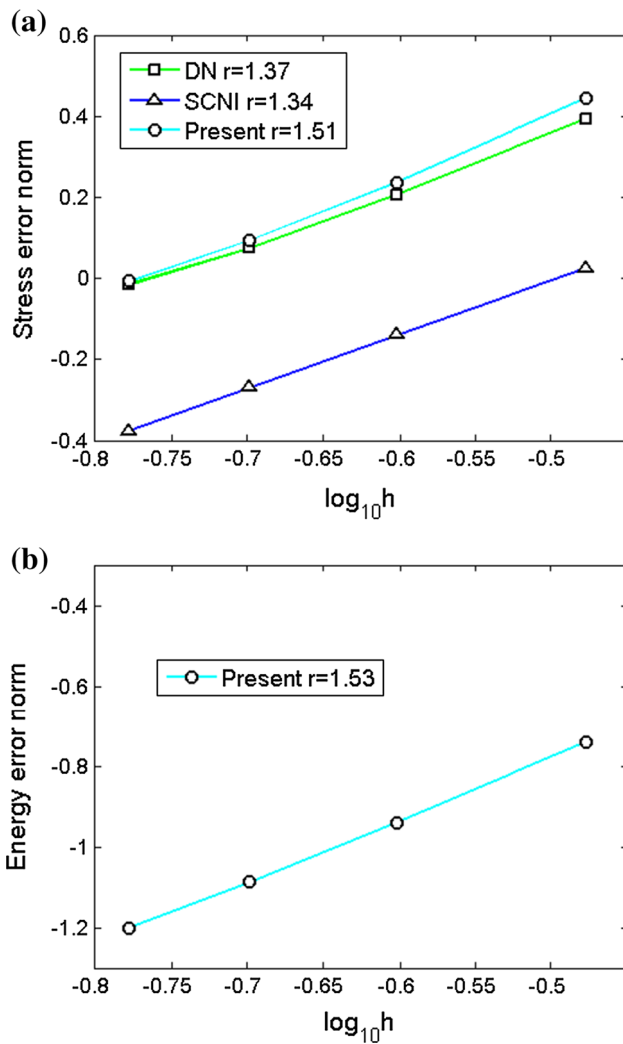


Fig. 4 Convergence plot. a Stress error $e_{\sigma\sigma}^h$, b energy error e_{ue}^h

low-energy modes in the solution, we observe comparable convergence order in the stress-error norm in this linear problem. Similar to the performance in GLS stabilization method [2], adding the present stabilization term into the direct nodal integration method may reduce the accuracy when the exact solution is relatively smooth and discretization is coarse. However, this inaccuracy decreases as the discretization is continuously refined. While the first-order of convergence is preserved in the stress-error norm of the present solution, the results in Fig. 4b have shown that the discretization solutions of stabilization term converge with the same rate in the energy-error norm e_{ue}^h . This numerical result indicates that the penalty error associated with the stabilization term decreases as fast as the error associated with the standard bilinear term when the exact solution is rather smooth. The scaled deformation plots are provided in Fig. 5a–c. The SCNI method appears to be the most accurate method among three comparison methods in this example.

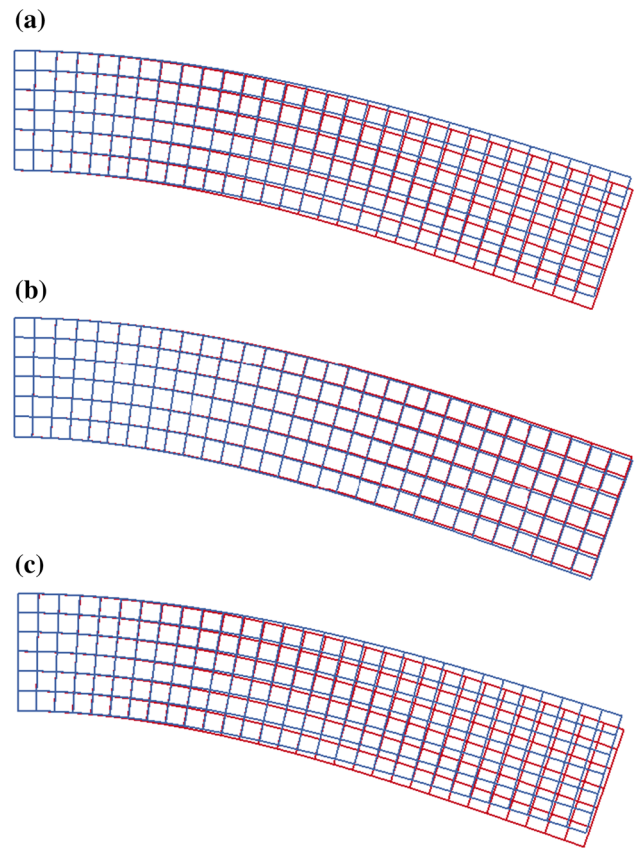


Fig. 5 Deformation plot (scaled by 5 times): analytical (red lines) and numerical (blue lines). a DN, b SCNI, c present method. (Color figure online)

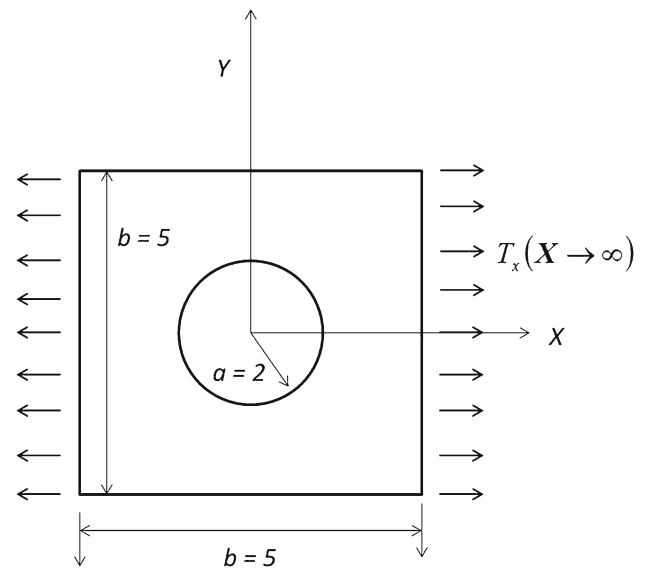


Fig. 6 Plate with a hole model

5.3 Infinite plate with a hole

An infinite plate with a center hole of radius $a = 2$ under uni-axial tension $T_x = 1$ as shown in Fig. 6 is considered

in this example. Based on the double symmetry of the problem, only the upper quadrant of the problem with boundaries Γ_h extended to $X = 5$ and $Y = 5$ is modeled. The material properties used in the analysis are the same as those in example 5.2. The analytical solution of the problem is available in [33]. Analytical solutions are applied along boundaries Γ_h , and zero normal displacements are prescribed on the symmetry boundaries. Since the discretization model contains the irregular nodal distribution, the non-uniform nodal support sizes are used in the analyses and they are defined by

$$\begin{aligned}
 \text{supp}(\Psi_I) &\equiv r_I = \sqrt{(r_{XI})^2 + (r_{YI})^2} \cdot r_n, \\
 r_{XI} &= \max_{J \in NN} (|X_I - X_J|), \\
 r_{YI} &= \max_{J \in NN} (|Y_I - Y_J|)
 \end{aligned}
 \tag{60}$$

where NN is the total number of neighboring nodes associated with the node I in a mesh setting using the finite element discretization, and r_n denotes the normalized nodal support size.

Figure 7a shows the convergence results in three comparison methods. The stress-error norm of present methods converges close to $O(h)$. In contrast, the optimal convergence order is not observed in the DN integration method. The non-convergent result of DN method is an outcome of low-energy modes residing in the solution as shown in Fig. 8a. Similar to the previous example, the SCNI method is very accurate in this problem. Compared with the DN method, the SCNI method and the present method are very stable as shown in Fig. 8b, c. The convergence of penalty error is shown in Fig. 7b. Since the analytical solution of this problem is comparatively non-smooth, the convergence rate of energy-error norm e_{ue}^h in the present method is slightly lower than that in the previous example.

5.4 2D punch problem

The displacement oscillation of nodal integration method is also investigated in the 2D punch test. A block of elastic material with a fixed bottom is punched by a rigid, frictionless and flat plate with a prescribed displacement. The elastic properties of the material are: Young’s modulus $E = 2.0E6$ and Poisson’s ratio $\nu = 0.3$. The model geometry is shown in Fig. 9. Five levels of uniform discretization in the model, namely 121 nodes, 441 nodes, 961 nodes, 1681 nodes and 2601 nodes, are utilized to study the convergence of the punch forces. The reference solution is obtained from a FEM analysis using the standard bilinear finite element formulation with a 3321-node model.

The convergence of punch force results is plotted in Fig. 10. As shown in the plot, the convergence in the direct nodal integration method is not uniform. This non-uniform

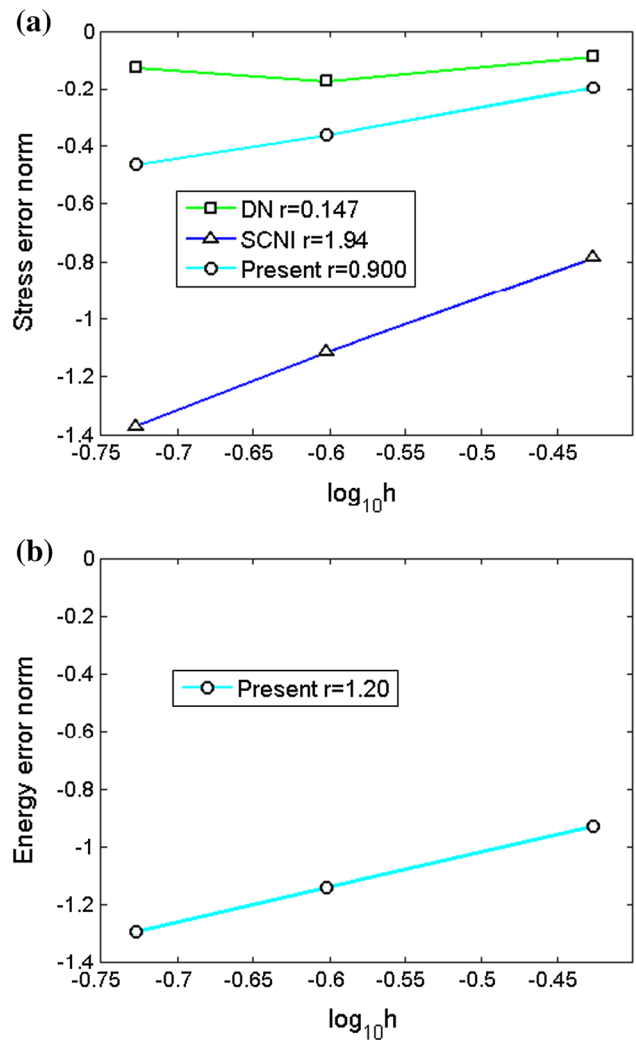


Fig. 7 Convergence plot. a Stress error $e_{\sigma\sigma}^h$, b energy error e_{ue}^h

convergence result is the cause of unstable deformation perturbed by the under-integration of weak form in the direct nodal integration method. Fig. 11a–e illustrate different perturbations of notorious low-energy modes observed in various discretization models. In comparison with the direction nodal integration method, standard SCNI method does not present the non-uniform convergence problem. However the convergence of the standard SCNI method is very slow in this punch test. As shown in Fig. 12a–e, the standard SCNI method exhibits different pattern of unstable modes in the deformation and the results are not improved when the model is continuously refined. The results of stabilized SCNI (SSCNI) formulation in Eq. (60) are also provided for the comparison. As shown in Fig. 10, the SSCNI method improves the SCNI method in terms of accuracy and convergence in this punch test. Figure 13a–e display the deformation plots of SSCNI method in various levels of discretization. Although slight oscillations of SSCNI solution are observed

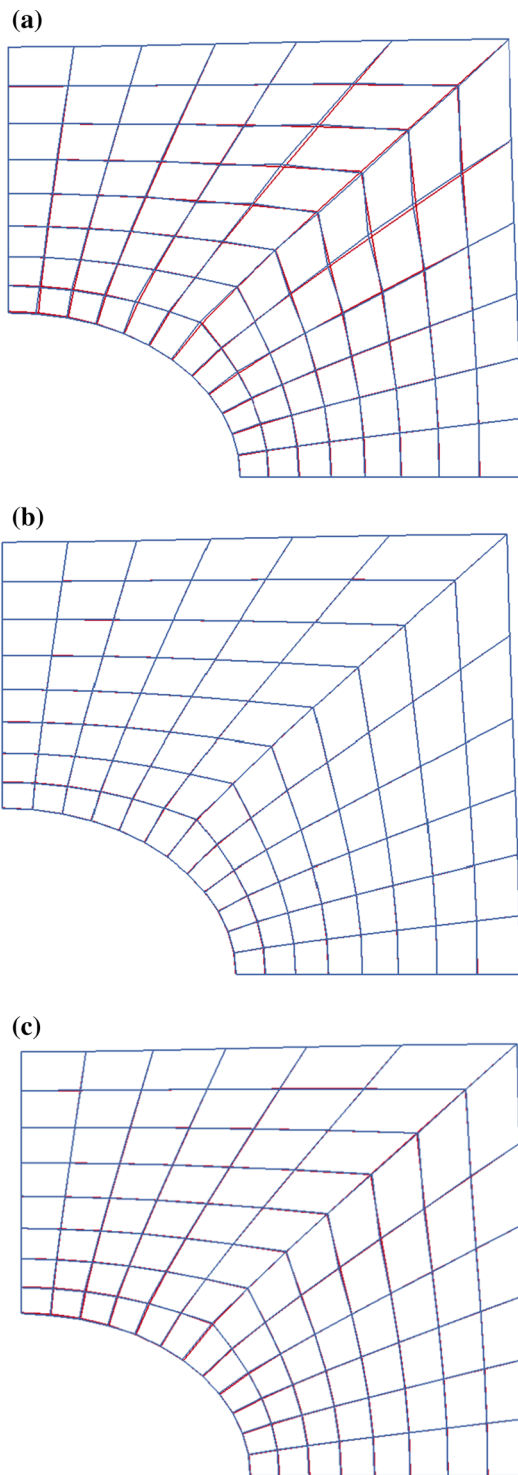


Fig. 8 Deformation plot (scaled by 100 times): analytical (*red lines*) and numerical (*blue lines*). **a** DN, **b** SCNI, **c** present method. (Color figure online)

in the first layer of nodes near the punch area, the unstable nodes inside the domain of SCNI model are effectively removed by the introduction of present strain gradient stabilization. On the other hand, the present method notably

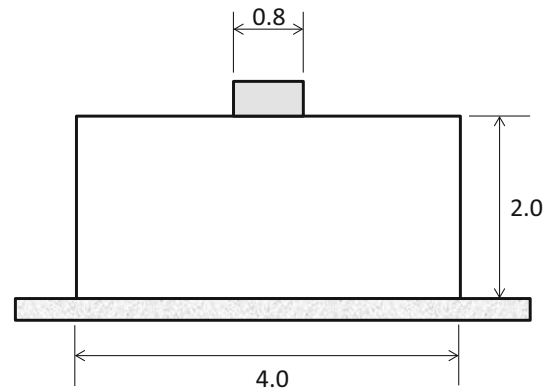


Fig. 9 Problem description for 2D punch model

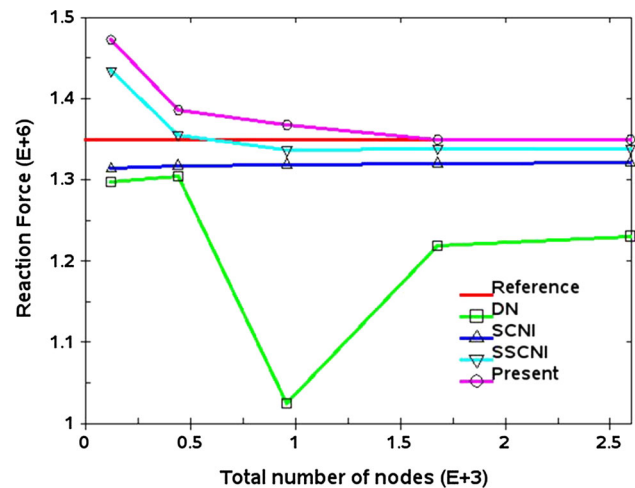


Fig. 10 Convergence of reaction force in 2D punch problem

improves the convergence of punch force over the other three methods. The deformation results in Fig. 14a–e imply the addition of a term penalizing the strain gradients to the direct nodal integration formulation can help stabilize the solution.

Two irregular models shown in Fig. 15a, b are created to test the performance of the present method under non-uniform discretization. Same nodal support size of that in the uniform discretization is used. Since both the standard SCNI method and the SSCNI method rely on the integration cells for computation, only the result of direction nodal integration method is reported for comparison. Figure 16a, b compare the deformation in the irregular model containing 441 nodes. Same comparison of irregular model containing 1681 nodes is given in Fig. 17a, b. The deformation plots in Figs. 16 and 17 indicate that the present method remains to produce a stable solution under the non-uniform discretization. While the accuracy of direct nodal integration method deteriorates in the non-uniform model as shown in Table 1, the present method is able to maintain high accuracy in the prediction of punch forces.

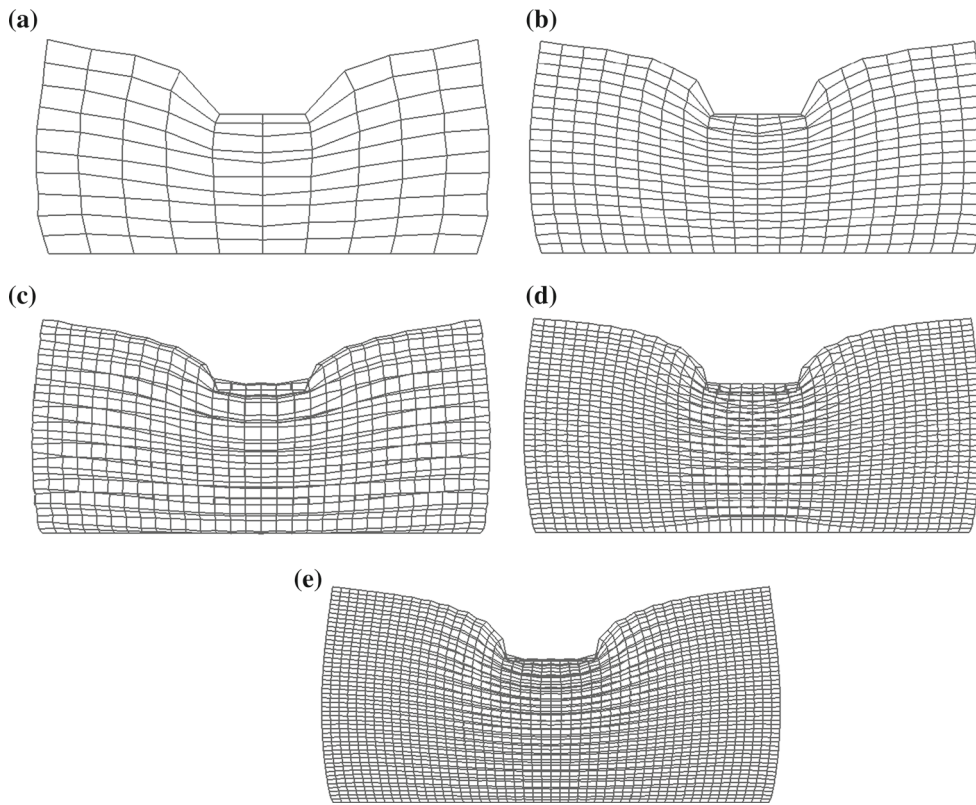


Fig. 11 Deformation plots for the direct nodal integration method. **a** 121 nodes, **b** 441 nodes, **c** 961 nodes, **d** 1681 nodes, **e** 2601 nodes

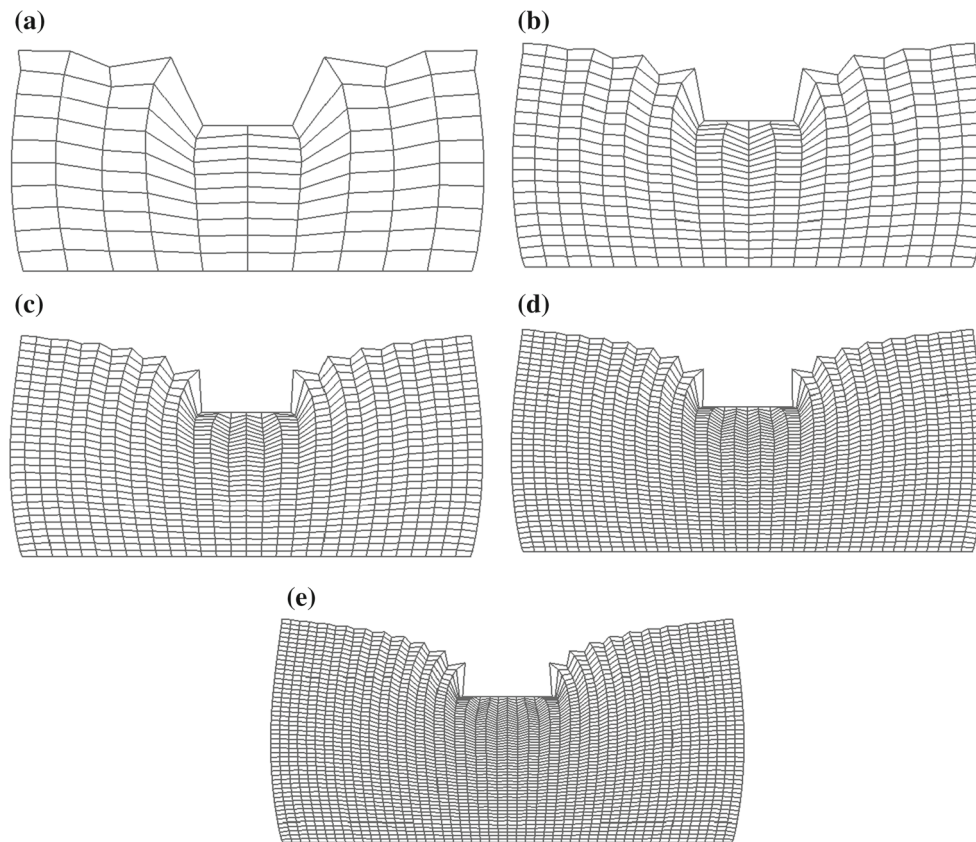


Fig. 12 Deformation plots for standard SCNI method. **a** 121 nodes, **b** 441 nodes, **c** 961 nodes, **d** 1681 nodes, **e** 2601 nodes

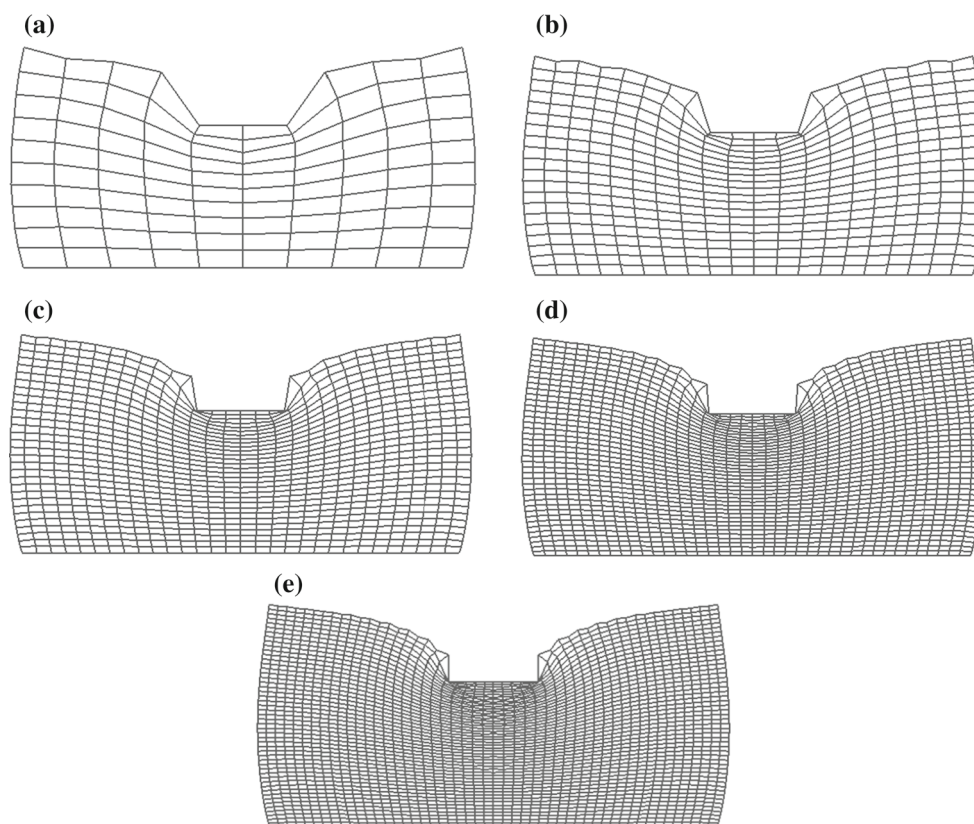


Fig. 13 Deformation plots for standard SSCNI method. **a** 121 nodes, **b** 441 nodes, **c** 961 nodes, **d** 1681 nodes, **e** 2601 nodes

5.5 The study of nodal support size effect

The solution sensitivity from the nodal support size effect is studied in this example. Same 2D punch problem in example 5.4 is considered. The uniform model containing 1681 nodes with a normalized support size varies from 2.2 to 3.6 is analyzed. As shown in Fig. 18, the direction nodal integration method produces noticeable error in the punch force and the result is highly sensitive to the nodal support size. Figures 19a and 20a depict the unstable deformation of the direct nodal integration method using the normalized support size of 2.2 and 3.6 respectively. On the other hand, the present method significantly improves the solutions over the direction nodal integration method, and the result is much less sensitive to the nodal support size. The non-sensitivity of the nodal support size effect in the present method also attributes to the similar displacement fields as displayed in Fig. 19b and 20b using two very different normalized nodal support sizes.

The solution sensitivity to the nodal support size effect is also investigated using the non-uniform model containing 1681 nodes. As shown in Fig. 21 for the punch force responses, the non-uniform model results of direction nodal integration method are in general softer than those in the uniform model for the tested nodal support sizes. This numerical

behavior of direct nodal integration method indicates that the notorious low-energy modes are more profound in the non-uniform model than that in the uniform model. It is also observed that the deformation profile of the direction nodal integration method in Fig. 22a and 23a is less symmetrical than it was shown in the uniform case. Apparently, the overall performance of direction integration method in the non-uniform discretization is less accurate than that in the uniform discretization. On the contrary, the present method generates the result which is less sensitive to the nodal support size. The deformation profiles of the present method in two severe nodal support sizes, 2.2 and 3.6 are quite comparable as shown in Fig. 22b and 23b respectively. Evidently, the spurious oscillations of the solution in the direct nodal integration method are effectively suppressed in the present solution thanks to the strain gradient stabilization.

6 Conclusion

In conventional penalty-type or residual-type stabilization approaches, the choice of stabilization parameters is critical to the success of numerical performance in meshfree Galerkin nodal integration method. In essence, the selection of stabilization control parameter is strictly problem depen-

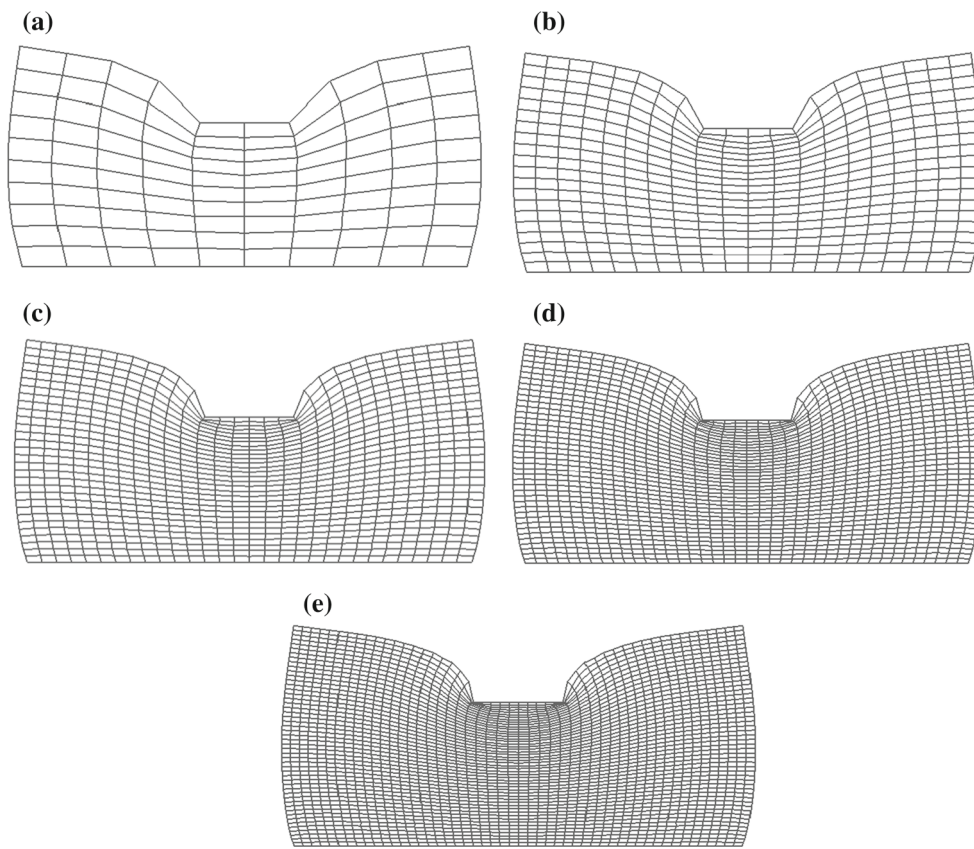


Fig. 14 Deformation plots for the present method. **a** 121 nodes, **b** 441 nodes, **c** 961 nodes, **d** 1681 nodes, **e** 2601 nodes

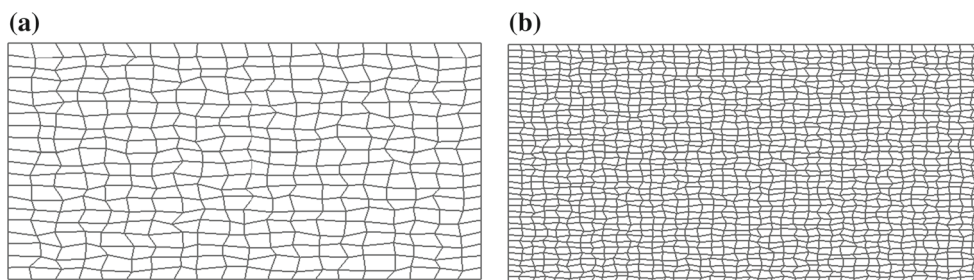


Fig. 15 Two irregular models in 2D punch problem. **a** 441 nodes, **b** 1681 nodes

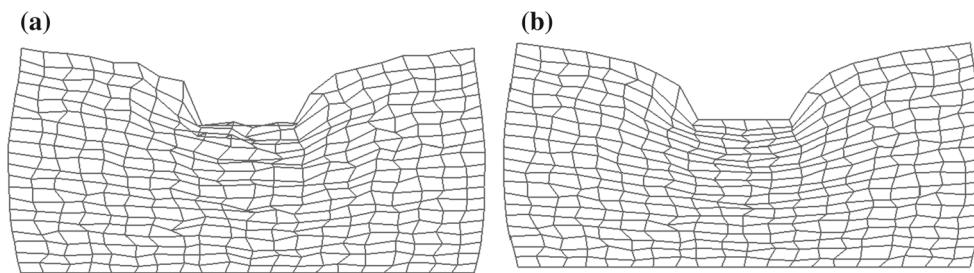


Fig. 16 Comparison of deformation in 441 nodes irregular model. **a** Direct nodal integration, **b** present method

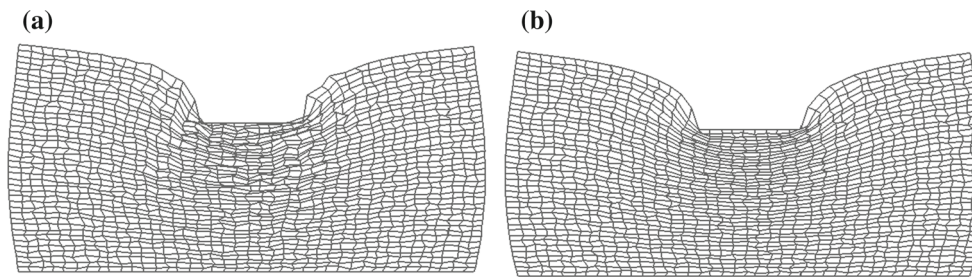


Fig. 17 Comparison of deformation in 1681 nodes irregular model. **a** Direct nodal integration, **b** present method

Table 1 Comparison of 2D punch forces in irregular models

	Direct nodal integration		Present	
	Regular	Irregular	Regular	Irregular
441 nodes	1.305e6	9.839e5	1.386e6	1.359e6
1681 nodes	1.219e6	1.121e6	1.351e6	1.349e6
Reference	1.351e6 (regular FEM 3321 nodes)			

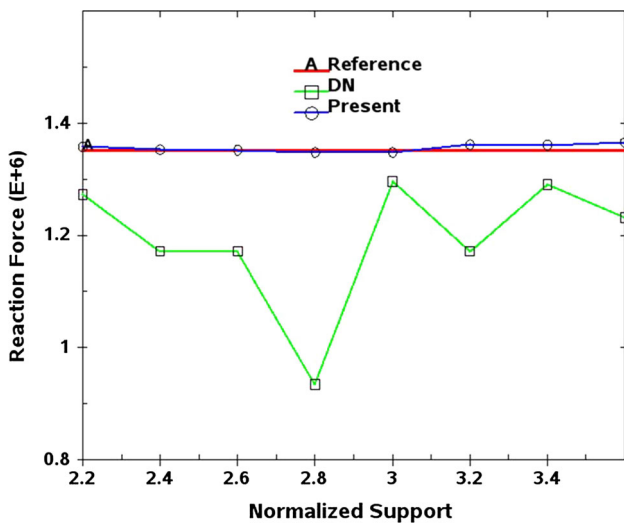


Fig. 18 Support size effect on the punch force response in 1681 nodes uniform model

dent and needs to be numerically calibrated. Additionally, the determination of characteristic length scale for stabilization is not obvious in the model containing irregular nodal distribution and/or using different nodal support sizes. In this study, we attempt to resolve those problems by presenting a strain gradient stabilization formulation. In the present formulation, the position-dependent stabilization parameter is derived from the displacement smoothing. It provides a simple way for effecting stabilization regardless of the irregularity of discretization and the variety of nodal support sizes. Since the stabilization formulation involves the second-order derivatives in displacement, it is considered as a type of strain gradient stabilization. The formulation is proven to pass the constant stress patch test if the SCNI scheme is performed to compute the standard bilinear term.

The numerical results of the present method indicate that the stress-error norm and the norm of penalty error are close to an optimal convergence rate of $O(h)$. The stabilization effect has been shown qualitatively in the 2D punch example in terms of stabilizing the spurious energy modes and predicting the correct force responses. Same numerical example also has been utilized to demonstrate the robustness of formulation. It has been shown that the resulting punch force is less sensitive to the variation of nodal support sizes and the irregularity of discretization. Theoretically, the present formulation does not require integration cells for the computation. Those nice features of present method could

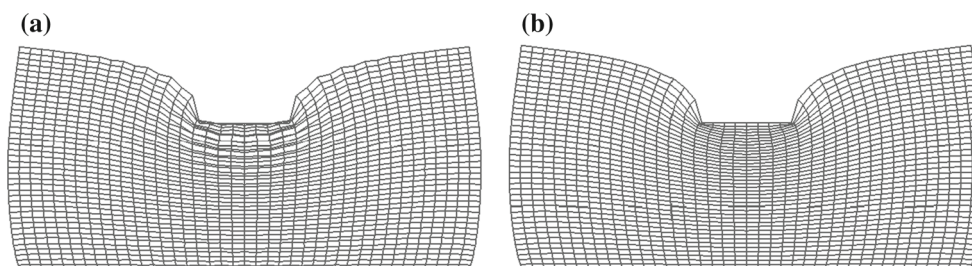


Fig. 19 Comparison of deformation in 1681 nodes uniform model with normalized support size equals to 2.2. **a** Direct nodal integration, **b** present method

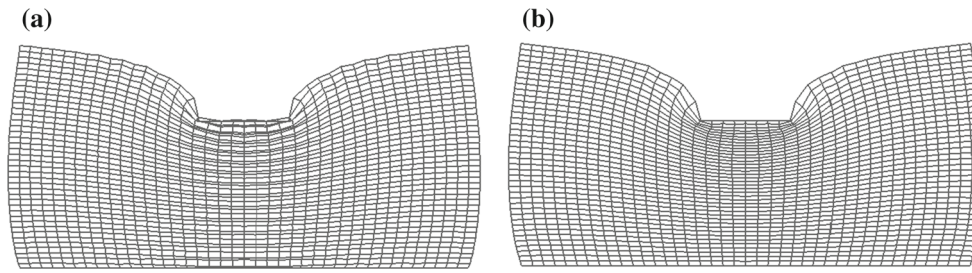


Fig. 20 Comparison of deformation in 1681 nodes uniform model with normalized support size equals to 3.6. **a** Direct nodal integration, **b** present method

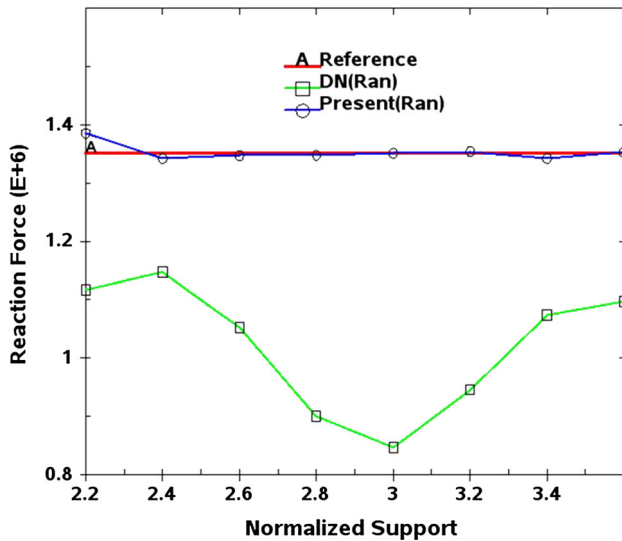


Fig. 21 Support size effect on the punch force response in 1681 nodes non-uniform model

offer an easier numerical implementation thus less computational complexity for the large deformation and failure simulation in solid mechanics applications. The development of stabilization formulation for nonlinear analysis is under investigation and will be addressed in the future.

Acknowledgments The authors would like to thank Dr. John O. Hallquist of LSTC for his support to this research. The support of this work by Yokohama Rubber Co, Ltd, Japan under the Yosemite Project is gratefully acknowledged.

Appendix

In this appendix, the derivation of stabilization gradient matrix for Eq. (47) is provided. First, let us recall the discrete smoothed displacement field to be approximated by

$$\bar{u}(X) = \hat{u}(X) + \tilde{u}(\hat{u}(X))$$

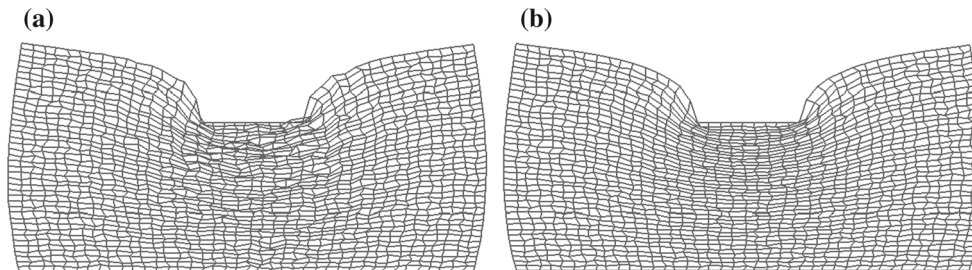


Fig. 22 Comparison of deformation in 1681 nodes non-uniform model with normalized support size equals to 2.2. **a** Direct nodal integration, **b** present method

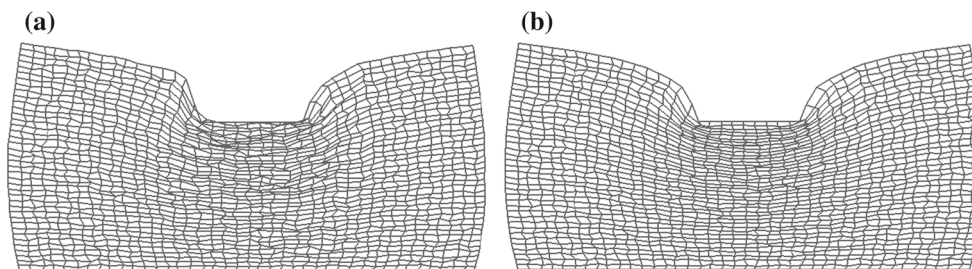


Fig. 23 Comparison of deformation in 1681 nodes non-uniform model with normalized support size equals to 3.6. **a** Direct nodal integration, **b** present method

$$= \sum_{I=1}^{NP} \Psi_I(\mathbf{X}) \hat{\mathbf{u}}(\mathbf{X}_I) + \left(\sum_{I=1}^{NP} \boldsymbol{\varepsilon}_I(\mathbf{X}) \right) \cdot^{(2)} \boldsymbol{\eta}(\mathbf{X}) \quad (61)$$

where

$$\boldsymbol{\eta}(\mathbf{X}) = \frac{1}{2} \begin{bmatrix} \sum_{I=1}^{NP} \tilde{\Psi}_I(\mathbf{X})(X_I - X)^2 & \sum_{I=1}^{NP} \tilde{\Psi}_I(\mathbf{X})(X_I - X)(Y_I - Y) \\ \sum_{I=1}^{NP} \tilde{\Psi}_I(\mathbf{X})(X_I - X)(Y_I - Y) & \sum_{I=1}^{NP} \tilde{\Psi}_I(\mathbf{X})(Y_I - Y)^2 \end{bmatrix} \quad (62)$$

$$\sum_{I=1}^{NP} \boldsymbol{\varepsilon}_I(\mathbf{X}) \approx \begin{bmatrix} \sum_{I=1}^{NP} \left(\Psi_{I,XX}(\mathbf{X}) + \Psi_{I,XY}(\mathbf{X}) \right) \hat{\mathbf{u}}_X(\mathbf{X}_I) \\ \sum_{I=1}^{NP} \left(\Psi_{I,YX}(\mathbf{X}) + \Psi_{I,YY}(\mathbf{X}) \right) \hat{\mathbf{u}}_Y(\mathbf{X}_I) \end{bmatrix} \quad (63)$$

Using Eqs. (61) ~ (63), the enhanced strain field in Eq. (37) is approximated by

$$\begin{aligned} \bar{\Theta}_h \boldsymbol{\varepsilon}(\hat{\mathbf{u}}) - \boldsymbol{\varepsilon}(\hat{\mathbf{u}}) &\approx \bar{\nabla}^{(2)} \hat{\mathbf{u}} \\ &= \frac{1}{2} \left(\nabla \boldsymbol{\eta} : \hat{\mathbf{u}} \nabla^{(2)} + \left(\nabla \boldsymbol{\eta} : \hat{\mathbf{u}} \nabla^{(2)} \right) \right) \\ &= \sum_{I=1}^{NP} \tilde{\mathbf{B}}_I(\mathbf{X}) \hat{\mathbf{u}}_I \end{aligned} \quad (64)$$

where

$$\tilde{\mathbf{B}}_I(\mathbf{X}) = \begin{bmatrix} \tilde{b}_{11} & \tilde{b}_{12} \\ \tilde{b}_{21} & \tilde{b}_{22} \\ \tilde{b}_{31} & \tilde{b}_{32} \end{bmatrix} \quad (65)$$

$$\tilde{b}_{11} = \chi_{XXX} \Psi_{I,XX} + \chi_{XXY} \Psi_{I,XY} \quad (66)$$

$$\tilde{b}_{12} = \chi_{XXY} \Psi_{I,XY} + \chi_{XXY} \Psi_{I,YY} \quad (67)$$

$$\begin{aligned} \tilde{b}_{21} &= \chi_{YXX} \Psi_{I,XY} + \chi_{XXY} \Psi_{I,XX} \\ &+ \chi_{YXX} \Psi_{I,XX} + \chi_{XXY} \Psi_{I,XY} \end{aligned} \quad (68)$$

$$\begin{aligned} \tilde{b}_{22} &= \chi_{YXY} \Psi_{I,YY} + \chi_{XYX} \Psi_{I,XY} \\ &+ \chi_{YXY} \Psi_{I,XY} + \chi_{XYX} \Psi_{I,YY} \end{aligned} \quad (69)$$

$$\tilde{b}_{31} = \chi_{YXY} \Psi_{I,XX} + \chi_{XYX} \Psi_{I,XY} \quad (70)$$

$$\tilde{b}_{32} = \chi_{YXY} \Psi_{I,XY} + \chi_{XYX} \Psi_{I,YY} \quad (71)$$

$$\chi_{XXX}(\mathbf{X}) = \frac{1}{2} \sum_{I=1}^{NP} \tilde{\Psi}_{I,X}(\mathbf{X})(X_I - X)^2 \quad (72)$$

$$\chi_{XXY}(\mathbf{X}) = \frac{1}{2} \sum_{I=1}^{NP} \tilde{\Psi}_{I,X}(\mathbf{X})(X_I - X)(Y_I - Y) \quad (73)$$

$$\chi_{YYX}(\mathbf{X}) = \frac{1}{2} \sum_{I=1}^{NP} \tilde{\Psi}_{I,Y}(\mathbf{X})(Y_I - Y)^2 \quad (74)$$

$$\chi_{YXY}(\mathbf{X}) = \frac{1}{2} \sum_{I=1}^{NP} \tilde{\Psi}_{I,Y}(\mathbf{X})(X_I - X)(Y_I - Y) \quad (75)$$

$$\chi_{YXX}(\mathbf{X}) = \frac{1}{2} \sum_{I=1}^{NP} \tilde{\Psi}_{I,Y}(\mathbf{X})(X_I - X)^2 \quad (76)$$

$$\chi_{XYY}(\mathbf{X}) = \frac{1}{2} \sum_{I=1}^{NP} \tilde{\Psi}_{I,X}(\mathbf{X})(Y_I - Y)^2 \quad (77)$$

References

- Arroyo M, Ortiz M (2006) Local maximum-entropy approximation schemes: a seamless bridge between finite elements and meshfree methods. *Int J Numer Methods Eng* 65:2167–2202
- Beissel S, Belytschko T (1996) Nodal integration of the element-free Galerkin method. *Comput Methods Appl Mech Eng* 139:49–74
- Belytschko T, Lu YY, Gu L (1994) Element-free Galerkin methods. *Int J Numer Methods Eng* 37:229–256
- Bochev PB, Gunzburger MD (1998) Finite element methods of least-squares type. *SIAM Rev* 40:789–837
- Brenner SC, Scott LR (2008) *The Mathematical Theory of Finite Element Methods*, 3rd edn. Springer, New York
- Chen JS, Pan C, Wu CT, Liu WK (1996) Reproducing kernel particle methods for large deformation analysis of non-linear structures. *Comput Methods Appl Mech Eng* 139:195–227
- Chen JS, Wu CT, Belytschko T (2000) Regularization of material instabilities by meshfree approximations with intrinsic length scales. *Int J Numer Methods Eng* 47:1303–1322
- Chen JS, Yoon S, Wang HP, Liu WK (2000) An improved reproducing kernel particle method for nearly incompressible finite elasticity. *Comput Methods Appl Mech Eng* 181:117–145
- Chen JS, Wu CT, Yoon S, You Y (2001) A stabilized conforming nodal integration for Galerkin meshfree methods. *Int J Numer Methods Eng* 50:435–466
- Chen JS, Yoon S, Wu CT (2002) Nonlinear version of stabilized conforming nodal integration for Galerkin meshfree methods. *Int J Numer Methods Eng* 53:2587–2615
- Chen JS, Hillman M, Rüter M (2013) An arbitrary order variationally consistent integration method for Galerkin meshfree methods. *Int J Numer Methods Eng* 95:387–418
- Donning B, Liu WK (1998) Meshless methods for shear deformable beams and plates. *Comput Methods Appl Mech Eng* 152:47–72
- Duan Q, Li X, Zhang H, Belytschko T (2012) Second-order accurate derivatives and integration schemes for meshfree methods. *Int J Numer Methods Eng* 92:399–424
- Franca LP, Hughes TJR (1993) Convergence analyses of Galerkin least-squares methods for symmetric advective-diffusive forms of the Stokes and incompressible Navier-Stokes equations. *Comput Methods Appl Mech Eng* 105:285–298
- Guan PC, Chi SW, Chen JS, Slawson Roth MJ (2011) Semi-Lagrangian reproducing kernel particle method for fragment-impact problems. *Int J Impact Eng* 38:1033–1047
- Günther FC, Liu WK (1998) Implementation of boundary conditions for meshless methods. *Comput Methods Appl Mech Eng* 163:205–230
- Hao S, Liu WK (2006) Moving particle finite element method with superconvergence: nodal integration formulation and applications. *Comput Methods Appl Mech Eng* 195:6059–6072
- Hillman M, Chen JS, Chi SW (2014) Stabilized and variationally consistent nodal integration for meshfree modeling of impact problems. *Comput Part Mech* 1:245–256

19. Hughes TJR, Brooks A (1982) A theoretical framework for Petro-Galerkin methods with discontinuous weighing functions: applications to the streamline upwind procedure. In: Gallagher RH, Carey GF, Oden JT, Zienkiewicz OC (eds) *Finite elements in fluids*, vol 4. Wiley, Chichester
20. Hughes TJR, Franca LP, Hulbert GM (1989) A new finite element formulation for computational fluid dynamics: VIII. The Galerkin/least-squares method for advective-diffusive equations. *Comput Methods Appl Mech Eng* 73:173–189
21. Li S, Liu WK (2004) *Meshfree particle method*. Springer, Berlin
22. Libersky LD, Petscheck AG, Carney TC, Hipp JR, Allahadai FA (1993) High strength Lagrangian hydrodynamics. *J Comput Phys* 109:67–75
23. Liu GR, Zhang GY, Wang YY, Zhong ZH, Li GY, Han X (2007) A nodal integration technique for meshfree radial point interpolation method (NI-RPIM). *Int J Solids Struct* 44:3840–3860
24. Liu GR (2010) *Meshfree methods: moving beyond the finite element method*. CRC Press, Florida
25. Liu WK, Ong JSJ, Uras RA (1985) Finite-element stabilization matrices—a unification approach. *Comput Methods Appl Mech Eng* 53:13–46
26. Liu WK, Jun S, Zhang YF (1995) Reproducing kernel particle methods. *Int J Numer Methods Fluids* 20:1081–1106
27. Park CK, Wu CT, Kan CD (2011) On the analysis of dispersion property and stable time step in meshfree method using generalized meshfree approximation. *Finite Elem Anal Des* 47:683–697
28. Puso MA, Chen JS, Zywick W, Elmer W (2008) Meshfree and finite element nodal integration methods. *Int J Numer Methods Eng* 74:416–446
29. Rabczuk T, Gracie R, Song HJ, Belytschko T (2010) Immersed particle method for fluid-structure interaction. *Int J Numer Methods Eng* 81:48–71
30. Simkins DC, Li S (2006) Meshfree simulations of thermal-mechanical ductile fracture. *Comput Mech* 38:235–249
31. Sukumar N (2004) Construction of polygonal interpolants: a maximum entropy approach. *Int J Numer Methods Eng* 61:2159–2181
32. Thomson LL, Pinsky PM (1995) A Galerkin least square finite element method for the two-dimensional Helmholtz equation. *Int J Numer Methods Eng* 38:371–397
33. Timoshenko SP, Goodier JN (1970) *Theory of elasticity*. McGraw-Hill, New York
34. Vignjevic R, Campbell J, Libersky LD (2000) A treatment of zero-energy modes in the smoothed particle hydrodynamics method. *Comput Methods Appl Mech Eng* 184:67–85
35. Wang DD, Chen JS (2004) Locking-free stabilized conforming nodal integration for meshfree Mindlin-Reissner plate formulation. *Comput Methods Appl Mech Eng* 193:1065–1083
36. Wang HP, Wu CT, Guo Y, Botkin M (2009) A coupled meshfree/finite element method for automotive crashworthiness simulations. *Int J Impact Eng* 36:1210–1222
37. Wu CT, Park CK, Chen JS (2011) A generalized approximation for the meshfree analysis of solids. *Int J Numer Methods Eng* 85:693–722
38. Wu CT, Hu W, Chen JS (2012) A meshfree-enriched finite element method for compressible and nearly incompressible elasticity. *Int J Numer Methods Eng* 90:882–914
39. Wu CT, Koishi M (2012) Three-dimensional meshfree-enriched finite element formulation for micromechanical hyperelastic modeling of particulate rubber composites. *Int J Numer Methods Eng* 91:1137–1157
40. Wu CT, Guo Y, Askari E (2013) Numerical modeling of composite solids using an immersed meshfree Galerkin method. *Composites B* 45:1397–1413
41. Wu CT, Hu W, Liu GR (2014) Bubble-enhanced smoothed finite element formulation: a variational multi-scale approach for volume-constrained problems in two-dimensional linear elasticity. *Int J Numer Methods Eng* 100:374–398
42. Wu CT, Guo Y, Hu W (2014) An introduction to the LS-DYNA smoothed particle Galerkin method for severe deformation and failure analysis in solids. In: 13th international LS-DYNA users conference, Detroit, MI, 8–10 June, pp 1–20
43. Wu YC, Wang DD, Wu CT (2014) Three dimensional fragmentation simulation of concrete structures with a nodally regularized meshfree method. *Theor Appl Fract Mech* 27:89–99